

Novel composites for microwave absorption

by

Nathan Lee Fischer

A thesis submitted to the graduate faculty
in partial fulfillment of the requirements for the degree of
MASTER OF SCIENCE

Major: Materials Science and Engineering

Program of Study Committee:
Nicola Bowler, Major Professor
Xiaoli Tan
Jaeyoun Kim

Iowa State University

Ames, Iowa

2008

Copyright © Nathan Lee Fischer, 2008. All rights reserved.

UMI Number: 1453127



UMI Microform 1453127

Copyright 2008 by ProQuest Information and Learning Company.
All rights reserved. This microform edition is protected against
unauthorized copying under Title 17, United States Code.

ProQuest Information and Learning Company
300 North Zeeb Road
P.O. Box 1346
Ann Arbor, MI 48106-1346

TABLE OF CONTENTS

LIST OF TABLES	iv
LIST OF FIGURES	v
CHAPTER 1. Introduction	1
1.1 Proposal	1
1.2 Uses of Microwaves	1
1.3 Absorption of Microwaves	2
1.3.1 Overview	2
1.3.2 Reflection Loss	2
1.4 Present Solutions	3
1.5 Proposed Solution	4
1.5.1 Polarization, Relaxation, and Resonance	5
1.5.2 Composite Modeling	8
1.5.3 Thin Film Conductivity	14
1.5.4 Effective Medium Theories	17
CHAPTER 2. Composite Fabrication and Characterization	19
2.1 Deposition Processes	19
2.1.1 Electroless Deposition	19
2.1.2 Sputter coating	21
2.2 Characterization Techniques	21
2.2.1 Electromagnetic Characterization	21
2.2.2 Pycnometry Measurements	26
2.2.3 X-Ray Diffraction	28

2.2.4	Particle Size Analysis	29
CHAPTER 3. Dielectric Composites for Microwave Absorption		30
3.1	Polydisperse Particles	30
3.1.1	Electroless Nickel-Coated Glass Microbubble	30
3.1.2	Sputtered Nickel-Coated Glass Microbubble	36
3.2	Monodisperse Particles	39
3.2.1	Electroless Nickel-Coated Glass Microsphere	39
3.3	Effective Medium Theory Comparison	46
3.3.1	Electroless Nickel-Coated Polydisperse Particles	46
3.3.2	Sputtered Nickel-Coated Polydisperse Particles	48
3.3.3	Electroless Nickel-Coated Monodisperse Particles	53
CHAPTER 4. Reflection Loss Comparison		57
4.1	Overview	57
4.2	Modeled Composite	57
4.3	Composite Exhibiting Dielectric Relaxation	59
4.4	Sputtered Nickel-Coated Glass Microbubble	59
4.5	Electroless Nickel-Coated Glass Microsphere	61
CHAPTER 5. Conclusion		65
REFERENCES		67
ACKNOWLEDGMENTS		71

LIST OF TABLES

Table 3.1	Parameters obtained by fitting Pseudo-Voigt function to XRD data of Ni-C15/250 microspheres	38
Table 3.2	Parameters obtained by fitting Pseudo-Voigt function to XRD data of nickel coated Mo-Sci microspheres	43
Table 3.3	Parameters used in Equation (1.17) to calculate real permittivity in Figure 3.26	50
Table 3.4	Parameters used to calculate permittivity in Figures 3.28 and 3.30 . .	51
Table 3.5	Parameters used to calculate permittivity in Figures 3.31 and 3.33 . .	54

LIST OF FIGURES

Figure 1.1	Example calculation of reflection loss for a non-magnetic, conductor-backed material with $\epsilon_r = 24 - i4$ and a thickness of 2mm	4
Figure 1.2	Example Debye relaxation with real (ϵ') and imaginary (ϵ'') parts of permittivity plotted	7
Figure 1.3	Example dielectric resonance with real (ϵ') and imaginary (ϵ'') parts of permittivity plotted with arbitrary units	8
Figure 1.4	Real relative permittivity calculated using Equations (1.15) and (1.16) for multiple conductivities at a volume fraction of 0.30	9
Figure 1.5	Imaginary relative permittivity calculated using Equations (1.15) and (1.16) for multiple conductivities at a volume fraction of 0.30	10
Figure 1.6	Real relative permittivity calculated using Equations (1.15) and (1.16) for multiple volume fractions with a conductivity of 1 S/m	10
Figure 1.7	Imaginary relative permittivity calculated using Equations (1.15) and (1.16) for multiple volume fractions with a conductivity of 1 S/m	11
Figure 1.8	Image of dispersed particles described by Sihvola and Lindell effective medium theory, Equation (1.17)	12
Figure 1.9	Effect of conductivity and metal thickness on relaxation frequency using Sihvola and Lindell effective medium theory, Equation (1.17)	13
Figure 1.10	Real relative permittivity calculated using Sihvola-Lindell effective medium theory, Equation (1.17), for multiple volume fractions of coated particles with $\epsilon_1 = 1 - i\frac{\sigma}{\omega\epsilon_0}$, $\epsilon_2 = 6.212 - i0.207$, a conductivity of 10^4 S/m, core radius (a_2) of $30\mu\text{m}$, and layer thickness of 15nm	13

Figure 1.11	Imaginary relative permittivity for same conditions as Figure 1.10 . . .	14
Figure 1.12	Effect of varying R in Equation (1.27)	16
Figure 3.1	SEM image of nickel coated S60 microspheres viewed with secondary electrons at a working distance of 45mm, an accelerating voltage of 20kV, a spot size of 48, and 500x magnification.	32
Figure 3.2	SEM image of nickel coated S60 microspheres viewed with secondary electrons at a working distance of 45mm, an accelerating voltage of 20kV, a spot size of 48, and 1400x magnification.	32
Figure 3.3	SEM image of nickel coated S60 microspheres viewed with secondary electrons at a working distance of 45mm, an accelerating voltage of 20kV, a spot size of 48, and 270x magnification.	33
Figure 3.4	Real permittivity for nickel coated S60 microspheres as a function of frequency and volume fraction	34
Figure 3.5	Imaginary permittivity for nickel coated S60 microspheres as a function of frequency and volume fraction	34
Figure 3.6	Real permeability for nickel coated S60 microspheres as a function of frequency and volume fraction	35
Figure 3.7	Imaginary permeability for nickel coated S60 microspheres as a function of frequency and volume fraction	35
Figure 3.8	Cumulative size distribution of the nickel coated C15/250 microspheres	37
Figure 3.9	XRD pattern of Ni-C15/250 particles	37
Figure 3.10	XRD pattern of Ni-C15/250 particles with background removed and fit using the Pseudo-Voigt function.	38
Figure 3.11	Measured ϵ' for a composite formed from nickel-coated C15/250 microspheres dispersed in paraffin wax, as a function of frequency and volume fraction	40

Figure 3.12	Measured ϵ'' for a composite formed from nickel-coated C15/250 microspheres dispersed in paraffin wax, as a function of frequency and volume fraction	40
Figure 3.13	Measured μ' for a composite formed from nickel-coated C15/250 microspheres dispersed in paraffin wax, as a function of frequency and volume fraction	41
Figure 3.14	Measured μ'' for a composite formed from nickel-coated C15/250 microspheres dispersed in paraffin wax, as a function of frequency and volume fraction	41
Figure 3.15	XRD pattern of nickel coated Mo-Sci particles	42
Figure 3.16	XRD pattern of nickel coated Mo-Sci particles with background removed and fit using a Pseudo-Voigt function.	43
Figure 3.17	SEM image of nickel coated Mo-Sci microspheres viewed with secondary electrons at a working distance of 48mm, an accelerating voltage of 15kV, a spot size of 49, and 100x magnification.	44
Figure 3.18	SEM image of nickel coated Mo-Sci microspheres viewed with secondary electrons at a working distance of 48mm, an accelerating voltage of 15kV, a spot size of 49, and 800x magnification.	45
Figure 3.19	SEM image of nickel coated Mo-Sci microspheres viewed with secondary electrons at a working distance of 48mm, an accelerating voltage of 15kV, a spot size of 49, and 1500x magnification.	45
Figure 3.20	Measured ϵ' for a composite formed from nickel coated Mo-Sci microspheres dispersed in paraffin wax, as a function of frequency and volume fraction	46
Figure 3.21	Measured ϵ'' for a composite formed from nickel coated Mo-Sci microspheres dispersed in paraffin wax, as a function of frequency and volume fraction	47

Figure 3.22	Measured μ' for a composite formed from nickel coated Mo-Sci microspheres dispersed in paraffin wax, as a function of frequency and volume fraction	47
Figure 3.23	Measured μ'' for a composite formed from nickel coated Mo-Sci microspheres dispersed in paraffin wax, as a function of frequency and volume fraction	48
Figure 3.24	Real permittivity for nickel coated S60 microspheres as a function of volume fraction with calculated permittivity values using Hanai-Bruggeman, Harfield, and Sihvola-Lindell EMTs, assuming no coating	49
Figure 3.25	Imaginary permittivity for nickel coated S60 microspheres as a function of volume fraction with calculated permittivity values using Hanai-Bruggeman, Harfield, and Sihvola-Lindell EMTs, assuming no coating	49
Figure 3.26	Real permittivity for nickel coated S60 microspheres as a function of frequency and volume fraction with calculated permittivity values using Equation (1.17) and Table 3.3	50
Figure 3.27	XRD pattern of electroless nickel-coated polydisperse particles	51
Figure 3.28	Experimental data taken at 3GHz on Ni-C15/250 microspheres in paraffin wax, compared with real permittivity calculated using the models of Sihvola-Lindell, Harfield, and Hanai-Bruggeman	52
Figure 3.29	Experimental data taken at 3GHz on Ni-C15/250 microspheres in paraffin wax, compared with imaginary permittivity calculated using the models of Sihvola-Lindell, Harfield, and Hanai-Bruggeman	52
Figure 3.30	Experimental real permittivity of Ni-C15/250 microspheres along with permittivity calculated using Equation (1.28) and parameters in Table 3.4	53
Figure 3.31	Experimental data taken at 3GHz on nickel coated Mo-Sci microspheres in paraffin wax, compared with real permittivity calculated using the model of Sihvola-Lindell, Harfield, and Hanai-Bruggeman	55

Figure 3.32	Experimental data taken at 3GHz on nickel coated Mo-Sci microspheres in paraffin wax, compared with imaginary permittivity calculated using the model of Sihvola-Lindell, Harfield, and Hanai-Bruggeman	55
Figure 3.33	Experimental real permittivity of nickel coated Mo-Sci microspheres along with permittivity calculated using Equation (1.28) and parameters in Table 3.5	56
Figure 4.1	Reflection loss contour for 0.50 volume fraction on model composite calculated using the Sihvola-Lindell model where $\epsilon_m=2.25(1-i2.5/10^4)$, $\epsilon_1=1-i\frac{\sigma}{\omega\epsilon_0}$, $\sigma=10^4$ S/m, $\epsilon_2=6.212-i0.207$, $a_1=30.015\mu\text{m}$, and $a_2=30\mu\text{m}$.	58
Figure 4.2	Minimum reflection loss for model composite described in section 1.5.2	58
Figure 4.3	Measured ϵ' for a composite formed from a hollow glass core, coated with tungsten and an outer layer of alumina, which exhibits dielectric relaxation [45]	59
Figure 4.4	Measured ϵ'' for a composite formed from a hollow glass core, coated with tungsten and an outer layer of alumina, which exhibits dielectric relaxation [45]	60
Figure 4.5	Reflection loss contour for 0.60 volume fraction of a composite with a hollow glass core, coated with tungsten and an outer layer of alumina, which exhibits dielectric relaxation	60
Figure 4.6	Minimum reflection loss for a composite a with hollow glass core, coated with tungsten and an outer layer of alumina, which exhibits dielectric relaxation for multiple volume fractions	61
Figure 4.7	Reflection loss contour for 0.46 volume fraction of nickel-coated C15/250 particles	62
Figure 4.8	Minimum reflection loss for nickel-coated C15/250 particles for multiple volume fractions	62
Figure 4.9	Reflection loss contour for 0.30 volume fraction of nickel-coated Mo-Sci particles	63

Figure 4.10	Minimum reflection loss for nickel-coated Mo-Sci particles for multiple volume fractions	64
-------------	---	----

CHAPTER 1. Introduction

1.1 Proposal

It is my goal through this research to bring forth experimental results and explanations for electromagnetic properties of materials composed of dielectric spheres coated with a thin layer of conductive material, dispersed in an inert matrix, which are thought to absorb microwave radiation by the process of interfacial polarization, as discussed in [1] and [2]. Particular attention will be given to the relationship between the metallic layer and resulting electromagnetic features.

1.2 Uses of Microwaves

Microwaves have found wide and varying use throughout society and industry. This technology is so pervasive that many use it daily, though few may realize this. This form of electromagnetic radiation is roughly defined as waves with a frequency between 1 and 40GHz. Current personal uses include cellular phones, wireless internet, and microwave ovens. With an estimated 243 million cellular phone users in the United States as of June 2007 [3], this technology has had a substantial effect on the daily lives of many people. The most popular mobile standard in the world, GSM, operates at 0.9 and 1.8GHz. Cell phones, in general, work by sending voice data in the form of microwaves to a base station while receiving data in the form of the voice of the person being called, at a different frequency. Microwave ovens heat food by supplying microwaves at a frequency of 2.45GHz. These waves are absorbed by water, fats, and sugars and largely ignored by the plastic, glass, or ceramic that contain the food. Wireless internet works in a similar fashion to a cellular phone, except computer data is transmitted instead of the voices of the operators. The most common wireless internet

standards are those defined by IEEE 802.11, with 802.11a operating at 5GHz, while 802.11b and 802.11g operate at 2.4GHz.

Industry has also found uses for microwave radiation in curing thermoset polymers [4] and long distance telecommunications. Thermoset polymers that are cured with an autoclave can receive an uneven curing if the object is large or if it has uneven dimensions. It has been proposed that this problem could be solved, and the curing process be completed more quickly, through the use of microwaves to produce the heating effect [5].

1.3 Absorption of Microwaves

1.3.1 Overview

With this wide-spread use of microwaves comes a desire to be able to control these electromagnetic waves more closely. The specific interest of this thesis is microwave absorption. However, the ability to absorb electromagnetic radiation in the microwave frequency range is an area where current technology lacks. A microwave absorbing product would prove to be very useful in the reduction of cross-talk in wireless telecommunication systems which use this frequency range, permitting higher power devices. Other applications include improving the heating distribution of microwaveable food packaging or in microwave-assisted curing of thermosets. The US military currently uses microwave absorbing technology in one of its stealth bombers, the B-2. This stealth bomber has a coating that absorbs radar waves [6], allowing the aircraft to operate without being detected by radar systems. These applications and many others could be imagined with this technology that has permeated many aspects of life.

1.3.2 Reflection Loss

When an electromagnetic wave is incident normally to a multilayer microwaving absorbing material that is assumed to have no conductivity, the wave impedance Z_i for the i th layer is given by [7]

$$Z_i = \eta_i \frac{Z_{i-1} + \eta_i \tanh(\gamma_i d_i)}{\eta_i + Z_{i-1} \tanh(\gamma_i d_i)} \quad (1.1)$$

$$\eta_i = \eta_o \sqrt{\frac{\mu_{ri}}{\epsilon_{ri}}} \quad (1.2)$$

$$\gamma_i = i \frac{2\pi f}{c} \sqrt{\mu_{ri} \epsilon_{ri}} \quad (1.3)$$

where ϵ_{ri} and μ_{ri} are the relative permittivity and permeability of the i th layer and η_o is the characteristic impedance of free space (377Ω). If a single layer of absorbing material is backed by a metal conductor, the impedance is given by

$$Z_1 = \eta_1 \tanh(\gamma_1 d_1) . \quad (1.4)$$

At the air-absorber interface, the reflection coefficient is given by

$$\Gamma = \left| \frac{Z_1 - \eta_o}{Z_1 + \eta_o} \right| \quad (1.5)$$

while the reflectivity in decibels is given by

$$R = 20 \log(\Gamma) . \quad (1.6)$$

The value of reflectivity, or reflection loss, is a function of frequency and material thickness via Equations (1.4) and (1.5). It is usually portrayed as a colormap with thickness as the ordinate and frequency as the abscissa or with a set thickness value, frequency as the abscissa, and reflection loss as the ordinate. A low reflection loss implies better absorption properties, with a minimum acceptable reflection loss for this method being -30dB, corresponding to 99.9% electromagnetic wave absorption [8]. An example calculation of reflection loss as a function of frequency is given as Figure 1.1.

1.4 Present Solutions

Currently, ferromagnetic filler particles, such as iron or cobalt, dispersed in a matrix are commonly used for absorption of microwave radiation [9]. This absorption takes place as a result of ferromagnetic resonance within the particles. Absorption can also be caused by magnetic domain movement in an alternating field, but this process occurs mainly in the megahertz range [10]. Ferromagnetic resonance is caused by strongly interacting electron spins in the ferromagnet [11]. These strong exchange forces result in a frequency or range

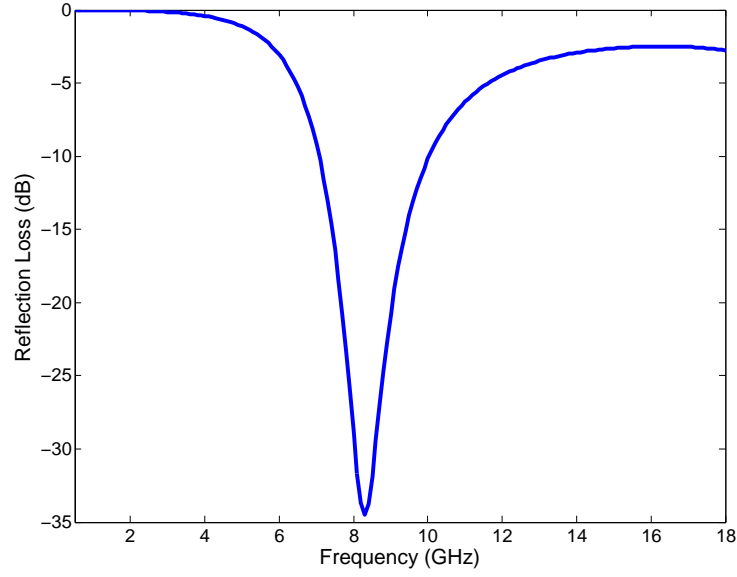


Figure 1.1 Example calculation of reflection loss for a non-magnetic, conductor-backed material with $\epsilon_r = 24 - i4$ and a thickness of 2mm

of frequencies where absorption of electromagnetic waves is greatly increased. The frequency where ferromagnetic resonance occurs, and its amplitude, are dependent upon the composition of the material, as well as its crystalline and magnetic structure [12]. In magnetic films, the thickness of the ferromagnetic film as well as induced eddy currents can also affect the location of the resonance.

As the high mass density of these metals can severely limit the usefulness of iron-based microwave absorbers, new materials for absorbing microwave range electromagnetic radiation should be developed.

1.5 Proposed Solution

Another method that can be used to absorb microwaves is to take advantage of a material's dielectric properties, rather than its magnetic properties. This is the basis of the present study. Absorption due to dielectric properties can either manifest itself in the phenomena of dielectric relaxation or resonance. Losses due to relaxation occur during transitions of charges or dipoles between two equilibrium positions separated by a potential barrier. Resonance occurs during

the displacement of charges elastically bound to an equilibrium position [13].

1.5.1 Polarization, Relaxation, and Resonance

When an external electric field is applied to an ideal dielectric material, there is no long range transfer of charge, but rather a movement of the internal charges to align themselves with the electric field, forming a dipole. The degree to which the dipoles align themselves to the electric field is called the material's polarizability. Different materials have different methods of polarization that are inherent in their structure. Ionic materials experience ionic polarization due to the slight movement of cations in the direction of the electric field and anions in the opposite direction. Orientational or dipolar polarization occurs in materials with permanent dipole moments, such as water or HCl, due to the dipole's alignment with the electric field. All materials experience electronic polarization, which occurs due to the electric field causing the center of the electron cloud to move away from the nucleus, causing the atoms to polarize. Interfacial polarization occurs whenever there is a buildup of charge at a boundary between two regions or materials. Crystal defects, such as dislocations or grain boundaries, electronic defects, or phase boundaries all contribute to interfacial polarization.

When dielectrics are placed in an alternating electric field, as opposed to the static one used to describe polarization mechanisms in the previous paragraph, their properties become frequency dependent. If the applied electric field is sinusoidal, the magnitude and direction of the field change with time. The dipoles from the mechanisms introduced earlier attempt to align themselves with the electric field as the field changes. At low frequencies, the dipoles are able to stay in phase with the electric field, aligning themselves as quickly as the field changes. As the frequency increases, the ability of the dipoles to align with the applied field decreases. In the case of orientational polarization, a polar molecule that rotates in a viscous medium, such as a liquid, interacts strongly with its neighbors thereby not allowing the dipole to align instantaneously with the applied field at frequencies above a certain characteristic frequency [14]. This delay brings about the lag that is experienced between the electric field and dipole. At high frequencies, the dipole is not able to align itself with the applied field at all and has

no contribution to the polarization within the material.

A general mathematical explanation of the frequency dependence of interfacial and orientational polarization, called dielectric relaxation, begins with the assumption that there is a finite amount of time required for dipoles in a dielectric to align with a static electric field, and an amount of time required to achieve random polarization once that field is removed. If the polarization before the electric field is applied is assumed to be zero and it increases to a final value exponentially, the time dependence of the polarization can be defined as

$$P(t) = P_{\infty} \left(1 - e^{-\frac{t}{\tau}}\right) \quad (1.7)$$

where $P(t)$ is the time dependent polarization, P_{∞} is the polarization at high frequency, t is time, and τ is the relaxation time, which is time independent but may be temperature dependent.

The rate of change of the polarization can be found by taking the derivative of Equation (1.7) with respect to time, forming

$$\frac{dP(t)}{dt} = \frac{1}{\tau} \left(P_{\infty} e^{-\frac{t}{\tau}}\right) \quad (1.8)$$

Inserting Equation (1.7) into Equation (1.8) results in

$$\frac{dP(t)}{dt} = \frac{1}{\tau} [P_{\infty} - P(t)]. \quad (1.9)$$

For a time-harmonic applied field, it can be shown that

$$P_{\infty} = (\epsilon_s - \epsilon_{\infty}) \epsilon_0 E_0 e^{i\omega t} \quad (1.10)$$

where ϵ_s is the permittivity in a static electric field, ϵ_{∞} is the high frequency permittivity, ϵ_0 is the permittivity of free space, E_0 is the magnitude of the applied field, and ω is the angular frequency of the applied field.

Integrating Equation (1.10) with respect to time yields

$$P(t) = C e^{-\frac{t}{\tau}} + \epsilon_0 \frac{(\epsilon_s - \epsilon_{\infty}) E_0 e^{i\omega \tau}}{1 + i\omega \tau}. \quad (1.11)$$

C is a constant and the term $C e^{-\frac{t}{\tau}}$ can be ignored when t is large compared to τ . Equation (1.11) can be shown to result in

$$\epsilon_r = \epsilon_{\infty} + \frac{\epsilon_s - \epsilon_{\infty}}{1 + i\omega \tau} \quad (1.12)$$

where ϵ_r is the complex permittivity and is also defined as

$$\epsilon_r = \epsilon'_r - i\epsilon''_r. \quad (1.13)$$

Equation (1.12) is called the Debye relaxation equation and is a general relationship to show how the permittivity of a dielectric changes with frequency of the applied electric field for polar liquids or in cases when interfacial polarization occurs. An example of Debye relaxation is shown as Figure 1.2. A more rigorous derivation of this equation can be found in [13] and [15].

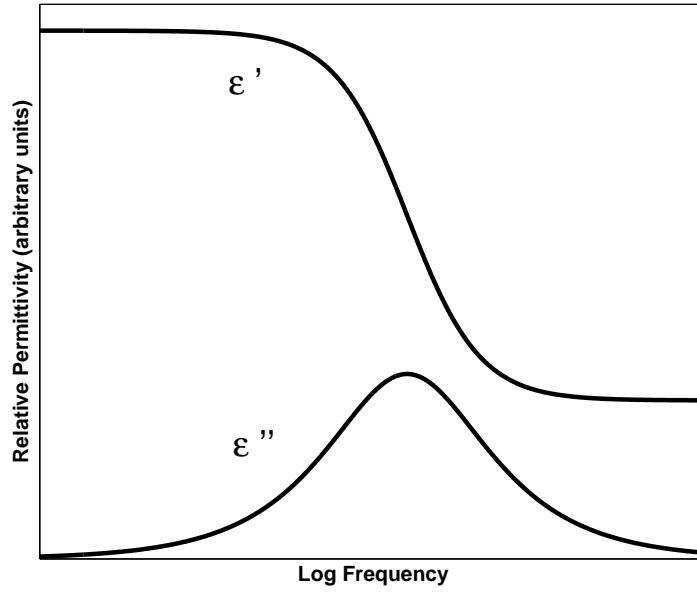


Figure 1.2 Example Debye relaxation with real (ϵ') and imaginary (ϵ'') parts of permittivity plotted

When considering dielectric resonance, which occurs in ionic and electronic polarization, the above equations do not hold. In this instance, it cannot be assumed that the polarization of the material reaches equilibrium exponentially with time, which was the assumption necessary for Equation (1.7). Instead, damped oscillations about the equilibrium polarization should be expected to occur with a frequency, known as the resonance frequency. Beginning with this assumption, it can be shown [13] that the complex permittivity can be described by

$$\epsilon(\omega) = \epsilon_\infty + \frac{\Delta\epsilon}{2} \left[\frac{1 - i\omega_0\tau}{1 - i(\omega_0 + \omega)\tau} + \frac{1 + i\omega_0\tau}{1 + i(\omega_0 - \omega)\tau} \right], \quad (1.14)$$

in which $\omega = 2\pi\nu$ is the angular frequency, $\omega_0 = 2\pi\nu_0$ is the resonance frequency, ϵ_∞ is the permittivity for $\omega \gg \omega_0$, τ is a time constant and $\Delta\epsilon = \epsilon_s - \epsilon_\infty$ is a polarizability term where ϵ_s is the permittivity for $\omega \ll \omega_0$. An example of dielectric resonance is given as Figure 1.3.

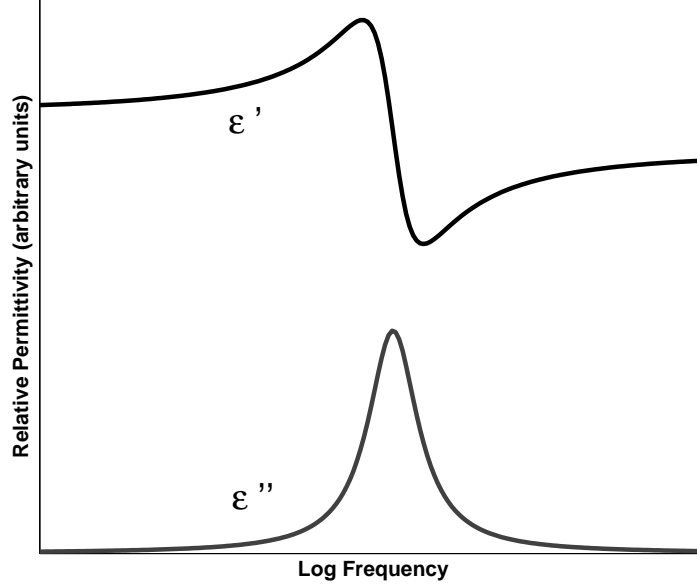


Figure 1.3 Example dielectric resonance with real (ϵ') and imaginary (ϵ'') parts of permittivity plotted with arbitrary units

1.5.2 Composite Modeling

A proposed method [16] of engineering dielectric relaxation due to interfacial polarization in the microwave frequency range is through the use of a composite material consisting of monodisperse, conductive particles in a non-conducting matrix. The interfacial polarization would occur due to a buildup of charges at the particle/matrix boundary. This system can be modeled through the use of the effective medium theory developed by J.C. Maxwell Garnett [17], which assumes a dilute solution of spherical inclusions randomly dispersed in a matrix. It states

$$\epsilon = \epsilon_m + 3v_f\epsilon_m \left[\frac{\epsilon_f - \epsilon_m}{\epsilon_f + 2\epsilon_m - v_f(\epsilon_f - \epsilon_m)} \right] \quad (1.15)$$

where ϵ is the effective permittivity of the composite, ϵ_m is the permittivity of the matrix, ϵ_f is the permittivity of the inclusions, and v_f is the volume fraction of the inclusions.

Paraffin wax dispersion-free in the microwave frequency range and is therefore a good material to use as the matrix material in as model system. According to von Hippel [18], the measured value of the permittivity for this material is $2.25(1 - i2.5/10^4)$ at 10GHz. For the conductive particles, the permittivity is frequency dependent and can be approximated from the Drude model for instances where $\omega\epsilon' \ll \sigma$ [19] as

$$\epsilon_f(\omega) = 1 - i \frac{\sigma}{\omega\epsilon_o} \quad (1.16)$$

where σ is the bulk dc conductivity of the conductor, and ϵ_o is the permittivity of free space (8.854×10^{-12} F/m).

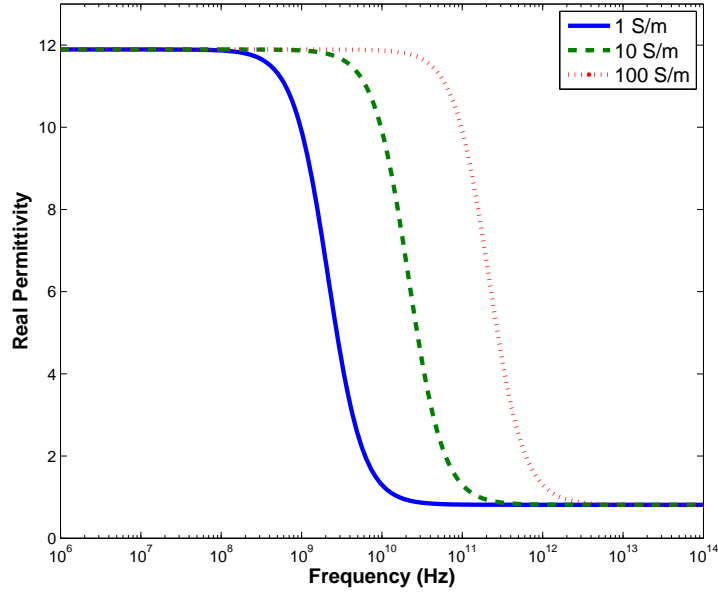


Figure 1.4 Real relative permittivity calculated using Equations (1.15) and (1.16) for multiple conductivities at a volume fraction of 0.30

In order to observe relaxation in the microwave frequency range, it was necessary to reduce the conductivity of the conductive particles between 1-100 S/m, as seen in Figures 1.4 and 1.5. The effect of volume fraction on the calculated permittivity can be seen in Figures 1.6 and 1.7, where the conductivity was set at 1 S/m.

Few materials have conductivities in the range of 1-100 S/m, which makes fabrication of this composite difficult. An alternative is to replace the low-conductivity particles with a non-conducting particle coated with a thin, highly conductive layer, such as a metal. Such particles

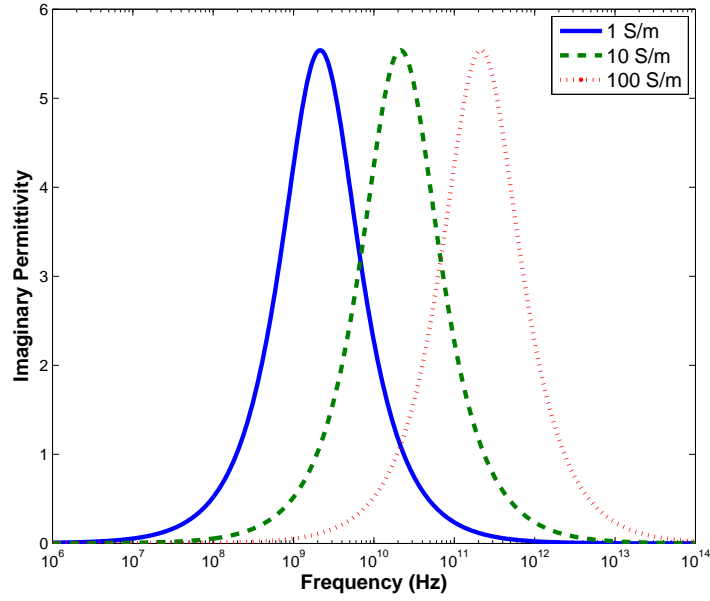


Figure 1.5 Imaginary relative permittivity calculated using Equations (1.15) and (1.16) for multiple conductivities at a volume fraction of 0.30

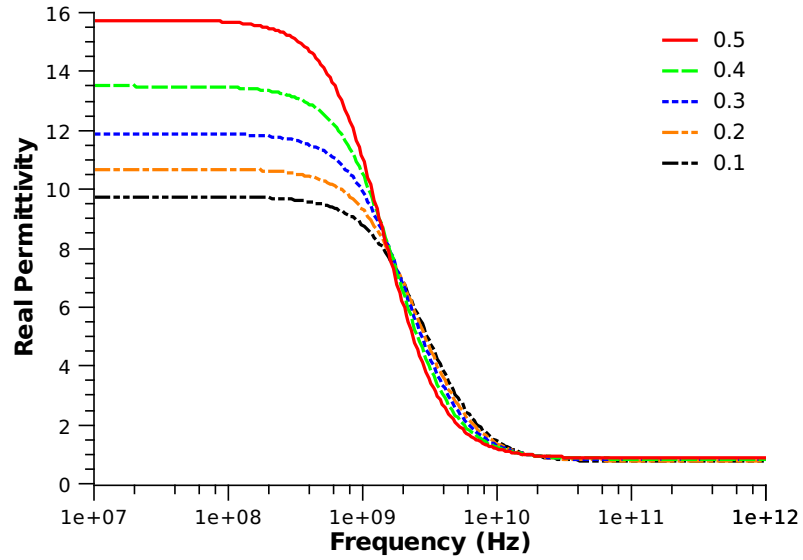


Figure 1.6 Real relative permittivity calculated using Equations (1.15) and (1.16) for multiple volume fractions with a conductivity of 1 S/m

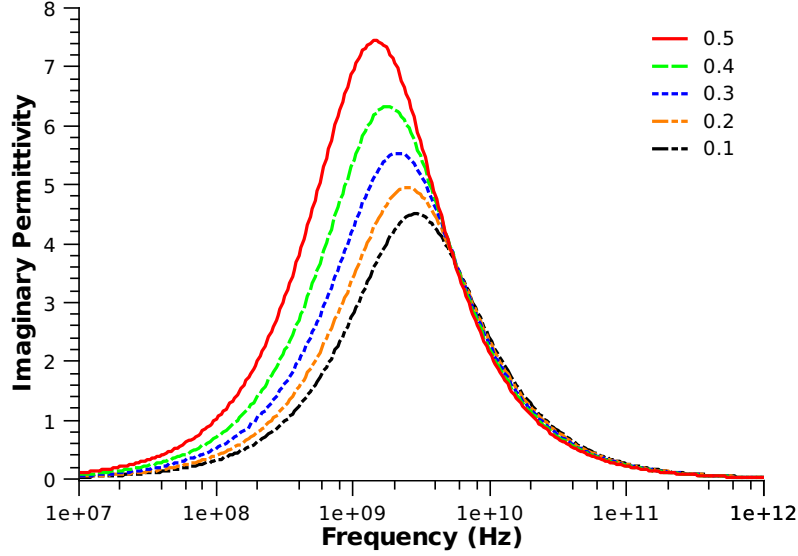


Figure 1.7 Imaginary relative permittivity calculated using Equations (1.15) and (1.16) for multiple volume fractions with a conductivity of 1 S/m

offer the possibility of low mass density, which would be attractive for aerospace applications or for the portability of telecommunications devices.

An equation describing the effective permittivity of spherical core-shell particles distributed in a matrix is given by Sihvola and Lindell [20] as

$$\frac{\epsilon - \epsilon_m}{\epsilon - 2\epsilon_m} = v_f \frac{(\epsilon_1 - \epsilon_m) + (2\epsilon_1 + \epsilon_m) g_N(\epsilon_k, a_k)}{(\epsilon_1 + \epsilon_m) + (2\epsilon_1 - \epsilon_m) g_N(\epsilon_k, a_k)} \quad (1.17)$$

where ϵ is the effective permittivity, ϵ_m is the permittivity of the matrix, v_f is the volume fraction of particles, a_k is the radius of the k th layer, ϵ_k is the permittivity of the k th layer of the particle, with ϵ_N being the innermost layer. A schematic of this type of particle is given as Figure 1.8. The function g_N is governed by the number of layers in the system and is given by,

$$g_2 = \frac{\epsilon_2 - \epsilon_1}{\epsilon_2 + 2\epsilon_1} \left(\frac{a_2}{a_1} \right)^3 \quad (1.18)$$

and

$$g_3 = \frac{(\epsilon_2 - \epsilon_1) \left(\frac{a_2}{a_1} \right)^3 + (2\epsilon_2 + \epsilon_1) \frac{\epsilon_3 - \epsilon_2}{\epsilon_3 + 2\epsilon_2} \left(\frac{a_3}{a_1} \right)^3}{\epsilon_2 + 2\epsilon_1 + 2(\epsilon_2 - \epsilon_1) \frac{\epsilon_3 - \epsilon_2}{\epsilon_3 + 2\epsilon_2} \left(\frac{a_3}{a_2} \right)^3}. \quad (1.19)$$

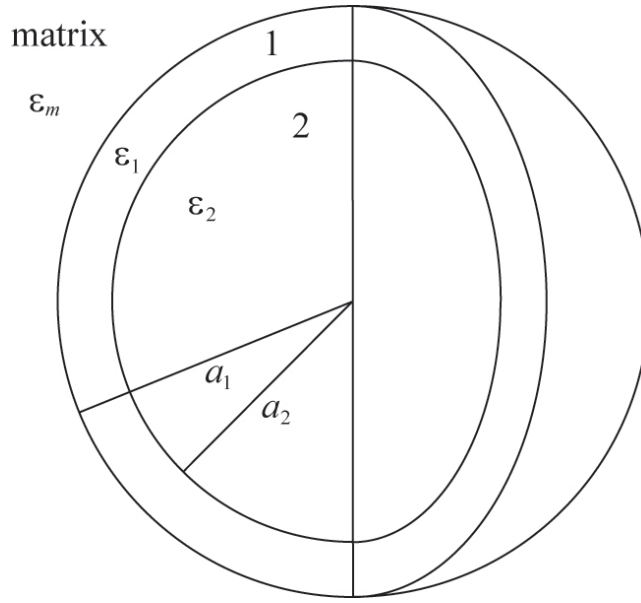


Figure 1.8 Image of dispersed particles described by Sihvola and Lindell effective medium theory, Equation (1.17)

The two parameters that play the most significant role in determining the precise frequency at which relaxation occurs are the conductivity of the metal layer and the ratio between the radius of the dielectric sphere and the thickness of the metal. The thickness of the metallic layer also plays a role in determining the conductivity of the metal, as layers of nanometric thickness do not have the same conductivity as the bulk material. Figure 1.9 shows the effect of conductivity and thickness of the metal layer on relaxation frequency, where a_2 is set to $30\mu\text{m}$ and ϵ_2 is $6.212-i0.207$ [21] for borosilicate glass. Figures 1.10 and 1.11 show the effect of volume fraction on the real and imaginary permittivity when $a_2=30\mu\text{m}$, $t=a_1 - a_2=15\text{nm}$, $\sigma=10^4$ S/m, and ϵ_2 is $6.212-i0.207$. As can be seen in these images, in order to see dielectric relaxation in the desired frequency range, a conductivity on the order of 10^4 S/m is necessary for the outer layer. While this is much less than the bulk conductivity of metals, which is on the order of 10^6 S/m, it is still possible to achieve these values for very thin metal layers. It has been shown [1][2] previously that nanometric layers of tungsten display the necessary conductivity values for dielectric relaxation to be observed in the microwave frequency range.

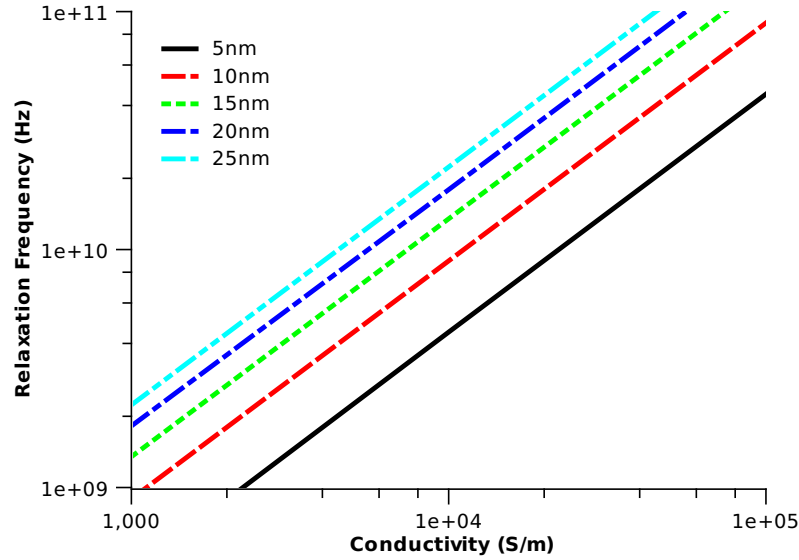


Figure 1.9 Effect of conductivity and metal thickness on relaxation frequency using Sihvola and Lindell effective medium theory, Equation (1.17)

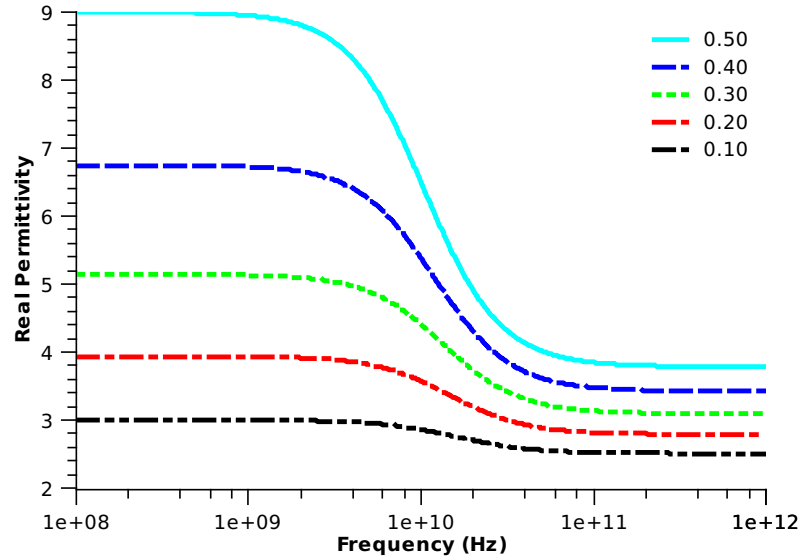


Figure 1.10 Real relative permittivity calculated using Sihvola-Lindell effective medium theory, Equation (1.17), for multiple volume fractions of coated particles with $\epsilon_1=1-i\frac{\sigma}{\omega\epsilon_0}$, $\epsilon_2=6.212-i0.207$, a conductivity of 10^4 S/m, core radius (a_2) of $30\mu\text{m}$, and layer thickness of 15nm

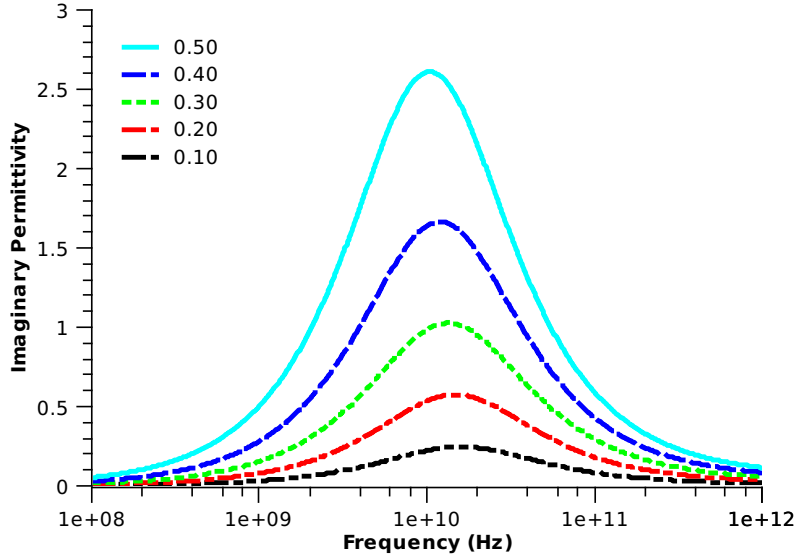


Figure 1.11 Imaginary relative permittivity for same conditions as Figure 1.10

1.5.3 Thin Film Conductivity

As the thickness of a metal layer decreases to the order of the mean free path of the conduction electrons, the major source of reduction in conductivity changes from scattering by phonons and defects in the crystal structure to scattering of the electrons by the surface of the film and grain boundaries.

Surface scattering of electrons is normally described by assuming that the electrons scatter inelastically and two collisions are necessary to randomize the velocity of an electron. If the solution to the Boltzmann transport equation is used as a starting point for the solution, the Fuchs-Sondheimer equation [22] can be derived, which states

$$\sigma_s = \sigma_o \left\{ 1 - \frac{3\lambda_o}{2t} \int_0^{\pi/2} \left[1 - \exp\left(-\frac{t}{\lambda_o} \cos \theta\right) \right] \sin^3 \theta \cos \theta d\theta \right\} \quad (1.20)$$

where σ_s is the conductivity of the thin film due to surface scattering, σ_o is the bulk conductivity, t is the film thickness, λ_o is the mean free path of the electrons in the bulk material, and p is the fraction of electrons reflected specularly. Published values of λ_o for Ni include 133Å [23] and 250Å [24].

When $t \gg \lambda_o$ and accounting for specular scattering, Equation (1.20) can be approximated to

$$\sigma_s \approx \sigma_o \left[1 + \frac{3\lambda_o}{8t} (1 - p) \right]^{-1} \quad (1.21)$$

In practice, Equation (1.21) is valid down to $\frac{D}{\lambda_o} \approx 0.3$ [14]. For $t \ll \lambda_o$, Equation (1.20) can be approximated to

$$\sigma_s \approx \sigma_o \frac{3t}{4\lambda_o} (1 + 2p) \left(\ln \frac{\lambda_o}{t} + 0.4228 \right) \quad (1.22)$$

In polycrystalline films, decreased conductivity is caused by grain boundary scattering more than by surface scattering [25]. Using a similar approach used to find the Fuchs-Sondheimer equations and assuming all scattering occurs at grain boundaries, the Mayadas-Shatzkes equation states

$$\sigma_g = \sigma_o \left[1 - \frac{3}{2}\alpha + 3\alpha^2 - 3\alpha^3 \ln \left(1 + \frac{1}{\alpha} \right) \right] \quad (1.23)$$

and

$$\alpha = \frac{\lambda_o}{D} \frac{R}{1 - R} \quad (1.24)$$

where σ_g is the conductivity due to grain scattering, D is the average grain diameter, and R is the probability of reflection of electrons at a grain boundary. Because it has been observed [26][27] that grains in a polycrystalline film are columns extending throughout the film, the average grain diameter, D , can be approximated as the film thickness.

In the limits of very small and very large values for α , Equation (1.24) simplifies to the following forms:

$$\sigma_g \approx \sigma_o \left[1 + \frac{3}{2}\alpha \right]^{-1} \quad (1.25)$$

for $\alpha \ll 1$, and

$$\sigma_g \approx \sigma_o \left[\frac{4}{3}\alpha \right]^{-1} \quad (1.26)$$

for $\alpha \gg 1$.

When analyzing thin films, both of these contributions are generally included through the use of Matthiessen's rule. This states that the effective resistivity of a material is the summation of resistivities from different scattering mechanisms. This analysis results in an

equation [28][24] describing the conductivity of a thin film of metal due to scattering by surfaces and grain boundaries when $\alpha \ll 1$ and $t \gg \lambda_o$

$$\sigma_{eff} \approx \sigma_o \left[1 + \frac{3\lambda_o}{8t} (1 - p) + \frac{3}{2}\alpha \right]^{-1}. \quad (1.27)$$

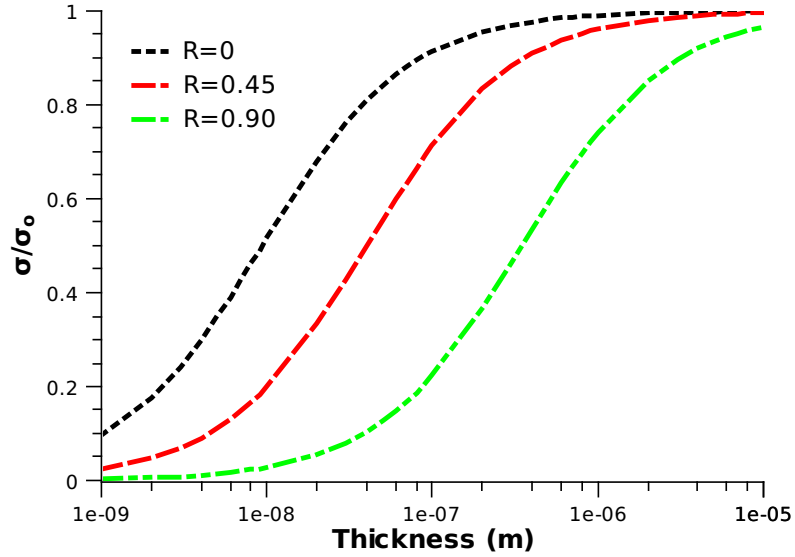


Figure 1.12 Effect of varying R in Equation (1.27)

Figure 1.12 plots Equation (1.27) as function of thickness and R . The mean free path was set to 250\AA while p was set to zero. As can be seen, an increase of the value for R moves the reduction in conductivity to higher thicknesses. An increase in the mean free path also results in the same shift, while an increase in the value of p causes a shift in the opposite direction. Neither a change in the mean free path nor in the value of p affect the shape of the conductivity curve as much as varying the value of R .

While these equations do appear to give good correlation between thickness and conductivity of a metal layer, they are almost exclusively used in instances where metal is evaporated onto flat substrates. Because the substrates in this investigation are curved, the usefulness of these equations for theoretical predictions depends on the curvature with respect to the film thickness. For a thin film with small curvature, these equations may be appropriate, but in this

investigation the curvature may be too great for these equations to apply. They do however, agree with the idea that very thin metal layers could result in the necessary conductivity values to observe dielectric relaxation in the microwave frequency range.

1.5.4 Effective Medium Theories

In composite materials, the bulk material properties are a mixture of the properties of its constituents. In order to predict the properties that result from this combination, effective medium theories, or EMTs, are used. Two EMTs for dielectric material have already been presented: the Maxwell Garnett and the Sihvola-Lindell theories. Two other EMTs that are useful in this investigation are those of Harfield [29] and Hanai-Bruggeman [30], modified for layered spherical particles.

The Harfield EMT assumes that the spherical, layered particles are arranged in a simple cubic lattice. The interactions between the particles are accounted for, treating each particle as a multipole source. This results in permittivity values that are generally higher than those calculated using the Sihvola-Lindell model for volume fractions greater than ≈ 0.30 .

The Hanai-Bruggeman model assumes that the Clausius-Mossotti formula holds true as small amounts of filler particles are continuously added to the composite. This accounts for a large distribution of particle sizes and is given by

$$\left(\frac{\epsilon - \beta_N \epsilon_1}{\epsilon_m - \beta_N \epsilon_1} \right) \left(\frac{\epsilon_m}{\epsilon} \right)^{1/3} = 1 - v_f \quad (1.28)$$

where N is the number of layers on the particle,

$$\beta_2 = \frac{\epsilon_2 + 2\epsilon_1 + 2(a_2/a_1)^3(\epsilon_2 - \epsilon_1)}{\epsilon_2 + 2\epsilon_1 - (a_2/a_1)^3(\epsilon_2 - \epsilon_1)} \quad (1.29)$$

and

$$\beta_3 = \frac{\left[\epsilon_2 + 2\epsilon_1 + 2(\epsilon_2 - \epsilon_1) \left(\frac{a_2}{a_1} \right)^3 \right] (\epsilon_3 + 2\epsilon_2) + 2 \left[(\epsilon_2 - \epsilon_1) \left(\frac{a_3}{a_2} \right)^3 + (2\epsilon_2 + \epsilon_1) \left(\frac{a_3}{a_1} \right)^3 \right] (\epsilon_3 - \epsilon_2)}{\left[\epsilon_2 + 2\epsilon_1 - (\epsilon_2 - \epsilon_1) \left(\frac{a_2}{a_1} \right)^3 \right] (\epsilon_3 + 2\epsilon_2) + \left[2(\epsilon_2 - \epsilon_1) \left(\frac{a_3}{a_2} \right)^3 - (2\epsilon_2 + \epsilon_1) \left(\frac{a_3}{a_1} \right)^3 \right] (\epsilon_3 - \epsilon_2)}. \quad (1.30)$$

The Maxwell Garnett, Sihvola-Lindell, Harfield, and Hanai-Bruggeman theories will be used in analysis presented in section 3.3 of fabricated particle composites that are described in Chapter 2.

CHAPTER 2. Composite Fabrication and Characterization

2.1 Deposition Processes

2.1.1 Electroless Deposition

Electroless deposition is a method of depositing a metal onto a wide variety of substrates. Some of the strengths of this method, as opposed to other metal deposition processes, are that it does not require the substrate to be conductive, deposits evenly over an entire surface, can be done using ordinary laboratory equipment, and is well documented. The deposition occurs as a reaction between a metal salt and a reducing agent, with other chemicals included to increase the stability of the reaction. After placing a substrate into a solution of a metal salt, a reducing agent, and other stabilizing chemicals, the substrate will act as a catalyst for the reducing agent. The reducing agent becomes oxidized at the surface of the substrate, which results in the production of electrons. These electrons combine with the metal ions in the solution to form neutral metal atoms on the surface of the substrate. As more atoms bond to the surface, a thin metal film will emerge. This then acts as an autocatalyst, which continues the deposition process [31].

The deposition begins in the form of an island of metal on the substrate surface, which grows laterally over the surface. This results in a metal layer with a small variation in thickness. The thickness of the metal layer is dependent upon the metal-ion concentration, the temperature of the solution, and the agitation of the solution. An increase in any of these parameters results in an increase in thickness [31].

The three most common chemicals used as reducing agents are sodium hypophosphite (NaH_2PO_2), sodium borohydride (NaBH_4), and dimethylamine borane (DMAB) [32]. Metals

that have been deposited with this method include Ni, Co, Pd, Cu, Ag, Au, Pt, Pb, Rh, and Ru, with Ni and Cu being the most common [31]. Electroless Ni deposition has found wide use in industry due to the wear and corrosion resistance of Ni [33]. Electroless Cu has found most of its use in printed circuit boards [34].

Before a non-conducting surface can undergo electroless deposition, it must go through a pretreatment step. The purpose of this step is to ensure the metal deposits on the intended surface and does not spontaneously form metal precipitates. After cleaning the surface of the sample with deionized water, it is immersed in a solution of tin(II) chloride (SnCl_2) and hydrochloric acid (HCl). The hydrochloric acid is included in the solution to prevent the formation of other tin compounds in the solution. The sample is then rinsed in water and placed in a solution of palladium chloride (PdCl_2) and hydrochloric acid, before being rinsed once more and finally placed in the deposition solution [35].

During the initial immersion in the tin(II) chloride solution, the tin compound is retained on the surface of the sample. During the palladium chloride immersion, palladium is reduced onto the remaining tin(II) chloride, and fine palladium particles form on the sample. The metal from the electroless deposition nucleates on these palladium particles before covering the entire sample surface [31].

According to [31] and [32], the three parameters that have the greatest effect on the deposition process are the concentration of the reducing agent, the temperature of the solution, and the pH of the solution. In this previous research, it has been shown that an increase in the concentration of the reducing agent increases the deposition rate and the concentration of elements from the reducing agent included in the metal deposit, namely boron or phosphorous. An increase in pH increases the deposition rate, but decreases concentration of boron/phosphorous in the film. An increase in the temperature of the solutions increases both the growth rate and the boron/phosphorous concentration in the deposited film.

The as-deposited film resembles a metal that has been rapidly quenched from a high temperature. If an adequate amount of a secondary element, usually from the reducing agent, such as boron or phosphorous, is included in the deposition, the film will potentially be nanocrystalline

or amorphous. The final crystal structure is dependent upon the solubility of the secondary element in the depositing metal and the presence of compounds of the two chemical species under equilibrium conditions.

2.1.2 Sputter coating

Sputtering is a deposition method where depositing atoms are ejected from a target that has been bombarded by ions [36]. Typically, argon is used for the ion source. The liberated atoms deposit evenly inside of the vacuum chamber, including onto the substrate. The crystallinity of the deposited film is heavily dependent upon the operating conditions of the sputterer. In order to evenly coat the particles investigated in this study, the particles were placed in a tumbler, which rotated while the sputtering deposition took place.

2.2 Characterization Techniques

2.2.1 Electromagnetic Characterization

2.2.1.1 Sample Preparation

Permittivity and permeability measurements were made on particles dispersed in a paraffin wax matrix. The samples used for the coaxial transmission line measurements had an outer diameter of 7mm, an inner diameter of 3mm, and a nominal height of 3mm. Using the density measurements made with a pycnometer, as described in section 2.2.2, the masses of filler particle and wax necessary to create samples with volume fractions ranging from 5% to 50% filler were calculated. These masses were measured out large enough to create a batch of ten samples and the two components were combined. This mixture was heated slightly above the melting point of the wax (65°C) until all of the wax became liquid. The batches were then removed from the hot plate and stirred continuously by hand until the wax solidified once again. This was done to try to achieve an even distribution of filler particles throughout the wax matrix. From these master batches, the appropriate amount of material was measured in order to create one sample and placed in a precision- machined mold. The mold was then

placed on a hot plate heated to 40°C for ten minutes while a 12kg lead brick was placed on top of the mold. This was done to remove gas as far as possible while not exceeding the crush pressure of the particles. Samples were removed from the mold, with any excess wax being removed with the use of a blade. The inside and outside diameters of the samples were measured with a caliper to ensure a good fit, while the heights of each individual sample were measured using a Fowler Ultra Digit Mark IV digital micrometer. The systematic uncertainty of the micrometer is one micron. Heights were measured at three approximately equidistant points, with the average being taken as the final value. The samples were then weighed before measurements were made.

2.2.1.2 Vector Network Analyzer

Measurements were made using an Anritsu vector network analyzer, model 37347C, using the transmission/reflection method. In this method, samples are placed in a waveguide or coaxial line and electromagnetic waves are directed toward the sample [37]. In these measurements the test port cables used are 7mm coaxial transmission lines and the sample holder is a Maury Microwave LPC7 7mm coaxial beadless airline. An analysis of the electric field at the interface of the sample results in scattering parameters, which can be interpreted to determine material properties of the system. The system used to take measurements included two ports for the generation and measurement of electromagnetic waves, so four scattering parameters, or S-parameters, were available. These values are commonly denoted as S_{ij} , where the i index denotes the port acting as the source of the electromagnetic wave, while the j index denotes the port measuring the electromagnetic wave. Therefore, parameters with similarly numbered subscripts are a measure of the electromagnetic waves returning back to its source, or reflected, while parameters with differently numbered subscripts are a measure of those passing through the sample, or transmitted.

2.2.1.3 S-Parameter Algorithms

The S-parameters by themselves give little information regarding the material properties of the sample being studied in the vector network analyzer. It is far more useful to have measurements on the frequency dependence of the permittivity and permeability of the material being studied. Therefore, a means of extracting this permittivity and permeability data from the S-parameter data is necessary. Nicolson and Ross [38], and Weir [39] developed a method to find both the permittivity and permeability of a sample as a function of the S-parameters, the sample height, and the sample's position within the airline. The NRW method, as it is commonly called, is not without its drawbacks, however. The solution becomes divergent at integral multiples of one-half wavelengths in the material. This is due to the scattering parameter $|S_{11}|$ becoming very small at these wavelengths, resulting in high uncertainty in the measurement of the phase. This dominates the solution, causing the divergence. In order to avoid this problem many researchers use samples shorter than one-half wavelength which incidentally also lowers the measurement sensitivity.

Another method was proposed by Baker-Jarvis [37], which takes advantage of a group of reference plane independent equations which he developed. The two most useful in the following investigation are given by:

$$\frac{S_{11}S_{22}}{S_{12}S_{21}} = \frac{(1 - \frac{\epsilon_r}{\mu_r})^2}{\frac{4\epsilon_r}{\mu_r}} \sinh^2 \gamma L \quad (2.1)$$

$$S_{12}S_{21} - S_{11}S_{22} = \exp[(-2\gamma_o)(L_{air} - L)] \frac{z^2 - \Gamma^2}{1 - z^2\Gamma^2} \quad (2.2)$$

where

$$\Gamma = \frac{\frac{c_o}{c_{lab}} \sqrt{\frac{\mu_r}{\epsilon_r}} - 1}{\frac{c_o}{c_{lab}} \sqrt{\frac{\mu_r}{\epsilon_r}} + 1} \quad (2.3)$$

$$z = \exp(-\gamma L) \quad (2.4)$$

$$\gamma = i \frac{\omega}{c_o} \sqrt{\mu_r \epsilon_r} \quad (2.5)$$

$$\gamma_o = i \frac{\omega}{c_{lab}} \quad (2.6)$$

and c_o is the speed of light in a vacuum, c_{lab} is the speed of light in the laboratory, i is $\sqrt{-1}$, ω is the angular frequency of the electromagnetic radiation, L is the length of the sample, L_{air} is the length of the airline, μ_r is the complex relative permeability, and ϵ_r is the complex relative permittivity. These equations have been simplified from those valid for a general transmission line and are valid only with the use of coaxial lines. For non-magnetic materials, the relative permeability can be assumed to be unity and either Equation (2.1) or (2.2) can be used to calculate the permittivity. A root-finding method, such as the Newton-Raphson technique, must be used point-by-point for each frequency to find the corresponding complex permittivity. The major advantage of this iterative technique over the NRW method is that it does not lead to the divergent behavior commonplace in the NRW method. This allows for the use of samples with a length greater than one-half wavelength, which results in lower uncertainty in the measurements [37]. For magnetic materials, the permeability cannot be assumed to be unity and both Equations (2.1) and (2.2) are required to find the complex permittivity and permeability. The two equations are solved simultaneously, point-by-point for each frequency, until the solutions over the entire frequency range are found. Like the NRW method, however, this technique is unstable at integral multiples of one-half wavelength in the material, limiting the thickness of samples used. The advantage of this technique over the NRW method is that it is independent of the sample position and results in smoother data.

Sources of error in these measurements arise from air gaps between the sample and sample holder, uncertainties in sample length and, for the NRW method, uncertainties in the sample position. Air gaps between the inner conductor and the sample or between the outer conductor and the sample cause a reduction in the measured permittivity due to the low value of permittivity for air. This effect is most pronounced if there is an air gap between the sample and the inner conductor because the electric field of the TEM mode is stronger at this point. The wax-based samples rarely suffer from the problem of air gaps since they are very slightly oversized when molded and then conform to the sample cell. Uncertainties in sample length

alter the measured value of permittivity and permeability because the sample length is used in the calculation of Equations (2.1) and (2.2). Because this can be easily known to a high degree of precision, it is not of major concern. Sample position is necessary in the calculation of permittivity and permeability in the NRW method and uncertainties in these values cause 'bending' in the values of permittivity [40]. Because the equations developed by Baker-Jarvis are position independent, this is not a source of error when these equations are used.

The periodic variations that are visible in some measurements are due to post-calibration mismatches which are introduced as connections are broken and re-made when samples are switched in the sample holder.

2.2.1.4 Higher Order Modes

When taking electromagnetic measurements in a coaxial waveguide it is generally desirable to have only a transverse electromagnetic, or TEM, mode propagating through the sample. In this mode, the magnetic field lines are concentric around the inner conductor while electric field lines are radial from the inner conductor, with no longitudinal field components. Other modes of propagation, such as transverse electric (TE) and transverse magnetic (TM), are also able to propagate under certain conditions, but these are not desirable in this study because the equations correlating S-parameters to permittivity and permeability assume that only a TEM mode is propagating through the sample. In order to prevent these modes from appearing, it is necessary to keep the wavelength of the signal within the waveguide below a critical wavelength, called the cutoff wavelength. The lowest order TM mode in the coaxial waveguide is the TM_{01} mode, which has a cutoff wavelength of [11]

$$\lambda_c^{TM} = 2(r_o - r_i), \quad (2.7)$$

while the lowest order TE mode, TE_{11} , has a cutoff wavelength of

$$\lambda_c^{TE} = \pi(r_o + r_i), \quad (2.8)$$

where r_o is the outer radius and r_i is the inner radius of the coaxial waveguide.

Since $\lambda_c^{TE} > \lambda_c^{TM}$, TE_{11} is the lowest frequency, higher order mode that may propagate in a coaxial line and is of primary concern in the prevention of the appearance of modes other than the TEM mode.

Because the value of the wavelength within the waveguide is dependent upon the permittivity and permeability of the material, there is a maximum value of these properties that if exceeded, results in the appearance of TE and TM modes in the waveguide. According to Baker-Jarvis [37], these modes can propagate in inhomogeneous samples with a relative permittivity greater than 10, and are be characterized by a sudden dip in $|S_{11}|$. In order to prevent these modes from propagating, samples with a thickness less than half of the guided wavelength can be used. For modes that are propagating at an angle to the axis of the coaxial cable, the effective sample length that the waves see is longer than the actual sample length, making the necessary sample thickness determination difficult.

2.2.2 Pycnometry Measurements

A pycnometer determines the volume of a sample by measuring the pressure difference when a known amount of gas under pressure is allowed to flow from a reference volume to the sample cell. After loading the sample, the system is at ambient pressure, and defined by

$$P_a (V_c - V_p) = n_a R T_a \quad (2.9)$$

where P_a is the ambient pressure, V_c is the volume of the sample cell, V_p is the volume of the sample, n_a is the moles of gas occupying the cell volume, R is the gas constant, and T_a is the ambient temperature.

The reference volume is then pressurized with gas from a cylinder to 17 pounds per square inch above ambient and the system can be defined by

$$P_1 V_R = n_1 R T_a \quad (2.10)$$

where V_R is the reference volume, P_1 is the pressure above ambient, and n_1 is the moles of gas in the reference volume.

When the gas is allowed to flow between the reference and sample cell, the system is defined by

$$P_2(V_C - V_P + V_R) = n_a RT_a + n_1 RT_a. \quad (2.11)$$

where P_2 is the pressure after connecting the cells.

Combining Equations (2.9), (2.10), and (2.11) yields

$$P_2(V_C - V_P + V_R) = P_a(V_C - V_P) + P_1 V_R \quad (2.12)$$

$$(P_2 - P_a)(V_C - V_P) = (P_1 - P_2)V_R \quad (2.13)$$

$$V_C - V_P = \frac{(P_1 - P_2)V_R}{(P_2 - P_a)}. \quad (2.14)$$

The ambient pressure is set to zero, creating

$$V_C - V_P = \frac{(P_1 - P_2)V_R}{P_2} \quad (2.15)$$

$$V_P = V_C - V_R \left(\frac{P_1}{P_2} - 1 \right) \quad (2.16)$$

V_C and V_R were found by placing two metal spheres of know volume in the pycnometer and measuring the pressures before and after connecting the reference volume and sample cell. The same measurements were then made without the metal spheres in the sample cell. Using this information, the volume of the reference and sample cells were calculated. The density of the powder is measured by dividing the mass of the powder by the calculated volume.

Using the measured densities of the particles before and after depositing metal, the approximate thickness of the metal layer can be found using

$$t_{shell} = \left[\frac{r_{core}^3 (\rho_{core} - \rho_{composite})}{\rho_{composite} - \rho_{shell}} + r_{core}^3 \right]^{1/3} - r_{core} \quad (2.17)$$

where t_{shell} is the thickness of the metal layer, ρ_{shell} is the density of the metal layer, r_{core} is the radius of the microspheres, ρ_{core} is the density of the microspheres, and $\rho_{composite}$ is the density of the microspheres after depositing the metal layer. Equation (2.17) assumes that the microspheres are monodisperse, all particles are perfect spheres, and the density of the deposited metal is the same value as that of the bulk metal.

Pycnometry measurements were made using a Quantachrome Multipycnometer, the micro sample holder, and helium gas at 17psi. The particles were then placed in the micro sample holder and the appropriate pressure measurements were taken, repeating the measurements until three consistent measurements in a row were made. The final volume was taken to be the average of these three readings. After this, the sample holder and powder were placed on an analytical balance and the mass recorded. The powder was then removed from the sample holder and the mass of the sample holder was taken. The difference between the two measurements was taken to be the mass of the powder.

2.2.3 X-Ray Diffraction

X-ray diffraction is a method of determining structural information of periodic, crystalline materials. In this study, it was used for qualitative phase and compositional identification as well as crystallinity determination. Because of the structure of crystalline solids, diffraction is possible at discrete angles of incident electromagnetic waves due to constructive interference. The angle of the incident wave and the spacing of the crystallographic planes are related by the Bragg equation,

$$n\lambda = 2d \sin \theta, \quad (2.18)$$

where λ is the wavelength of the electromagnetic radiation, d is the spacing between crystallographic planes, and θ is the angle between the plane and the incident wave. For cubic material, the relationship between plane spacing and lattice parameter is given by [41]

$$d = \frac{a}{\sqrt{h^2 + k^2 + l^2}}. \quad (2.19)$$

In order to extract useful information from the X-ray diffraction pattern, peaks are sometimes fitted to empirical equations. In this investigation, peaks were fitted to the Pseudo-Voigt function, which is a sum of Gaussian and Lorentzian equations and given by [41]

$$y(x) = \eta \frac{C_L^{1/2}}{\pi H} (1 + C_L x^2)^{-1} + (1 - \eta) \frac{C_G^{1/2}}{\sqrt{\pi} H} \exp(-C_G x^2), \quad (2.20)$$

where H is the full width at half maximum, $C_G = 4 \ln 2$, $C_L = 4$, and x is the distance from the center of the peak divided by H .

For all of the experiments in this discussion, a Scintag XGEN-400 diffractometer was used with a copper source with a wavelength of 1.540562Å.

2.2.4 Particle Size Analysis

The size distribution of a collection of particles can be determined using a particle size analyzer. These machines work by taking advantage of liquid-phase sedimentation and measure the change in particle concentration using light transmission either through gravitational or centrifugal sedimentation. As well as showing the distribution of diameters for a system of particles, the average diameter and standard deviation can be determined. If the values given are for the cumulative size distribution, $Q_N(x)$, the fractional size distribution function, $q_N(x)$, is equal to [42]

$$q_N(x) = \frac{d}{dx} Q_N(x). \quad (2.21)$$

If q_N is expected to be a normal distribution, it is given by

$$q_N(x) = \frac{1}{s\sqrt{2\pi}} \exp \left[-\frac{(x - \bar{x})^2}{2s^2} \right] \quad (2.22)$$

where \bar{x} is the average particle diameter and s is the standard deviation. These values are then given by

$$\bar{x} = \frac{\int_{-\infty}^{\infty} x q_N(x) dx}{\int_{-\infty}^{\infty} q_N(x) dx} \quad (2.23)$$

and

$$s = \left[\frac{\int_{-\infty}^{\infty} x q_N(x) (x - \bar{x})^2 dx}{\int_{-\infty}^{\infty} q_N(x) dx} \right]^{1/2}. \quad (2.24)$$

Therefore, if a cumulative size distribution can be acquired for a particular system of particles, the average diameter as well as the standard deviation of the diameter can be determined.

CHAPTER 3. Dielectric Composites for Microwave Absorption

3.1 Polydisperse Particles

3.1.1 Electroless Nickel-Coated Glass Microbubble

3.1.1.1 Overview

The first batch of particles created were 3MTM S60 glass microspheres coated in electrolessly deposited nickel. The S60 glass spheres are hollow, thin-walled, soda-lime-borosilicate glass spheres. They have a mean diameter of $30\mu\text{m}$, as given by the manufacturer, and a density of 0.584 g/cm^3 , which was determined using pycnometry, as explained in section 2.2.2. One gram of the S60 particles were placed in 100mL of a 0.1M HCl and 0.116M SnCl_2 solution at 50°C for 10 minutes. The solution was in an Erlenmeyer flask that was placed on a hot plate. A magnetic stir bar was placed in the solution and rotated by the hot plate. This stirring was used during every step of the deposition. The particles were filtered out of the solution by pouring the solution into a Buchner funnel that contained filtering paper and was attached to a filtering flask connected to a vacuum. When a vacuum was applied to the filtering flask, solution in the Buchner funnel would move through the filter paper and into the filtering flask, leaving the S60 particles on the surface of the filter paper. The filter paper used was Whatman #1, which retains particles larger than $11\mu\text{m}$ on the surface of the paper.

After the particles were filtered, they were scraped off the top of the filter paper, using a microspoon. The particles were then placed in an Erlenmeyer flask containing 100mL of a 0.1M HCl and 3.4mM PdCl_2 solution at 50°C for 10 minutes. The solution was stirred and filtered in the same manner as before.

The particles were then placed in an Erlenmeyer flask containing 200mL of a 0.342M glycolic

acid (HOCH_2COOH), 0.122M sodium acetate (CH_3COONa), 0.051M dimethylamine borane (DMAB), and 0.114M nickel sulfate (NiSO_4) solution, with continuous stirring. The solution was kept at a temperature of around 80°C and a pH of 4.1, which was regulated through the addition of sodium hydroxide (NaOH) to the solution when necessary. Temperature and pH were measured using a Oakton Acorn pH 5 meter with a double junction, glass electrode and temperature probe. Care had to be taken when making temperature measurements, as the metal temperature probe would have nickel deposited upon it after insertion into the solution. The temperature probe could not then be left in the solution, but only inserted for a short period of time to take measurements. The solution was allowed to react for one hour before filtering out the particles. The filter paper was then allowed to dry overnight and the particles were removed from the filter paper.

In order to analyze the surface finish of the nickel layer that resulted from the electroless deposition, the particles were viewed under a scanning electron microscope (SEM). A piece of carbon tape was placed on the electron beam target and the particles were placed on the carbon tape. Excess particles were removed from the target. As can be seen in Figure 3.1, the S60 substrate particles were not monodisperse and layers are clearly visible on the microspheres. This is even more clearly seen in Figure 3.2. These images show that the nickel coating appears to be continuous, but not even. The electroless deposition has resulted in a rough surface, with some regions having a thicker nickel layer than others. There also appeared to be regions where multiple microspheres would group together to form a large agglomerate, as seen in Figure 3.3. It is not known whether these groupings form during the deposition step or during the filtering process, but their existence results in undesirable electromagnetic properties. This problem was mostly eliminated by placing the filter paper in a glass petri dish that was heated above 100°C instead of allowing the filter paper to dry overnight.

When the microspheres are grouped together as such, electrons have a much larger path through which they can move when an alternating electric field is applied. This will not lead to the dielectric relaxation desired, but lead the material to act more like a conductor, which would not exhibit any relaxation.

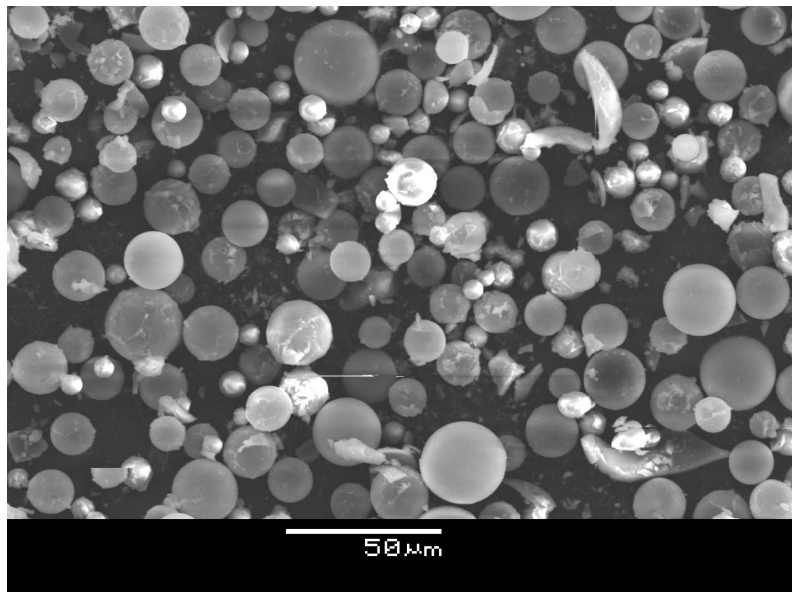


Figure 3.1 SEM image of nickel coated S60 microspheres viewed with secondary electrons at a working distance of 45mm, an accelerating voltage of 20kV, a spot size of 48, and 500x magnification.

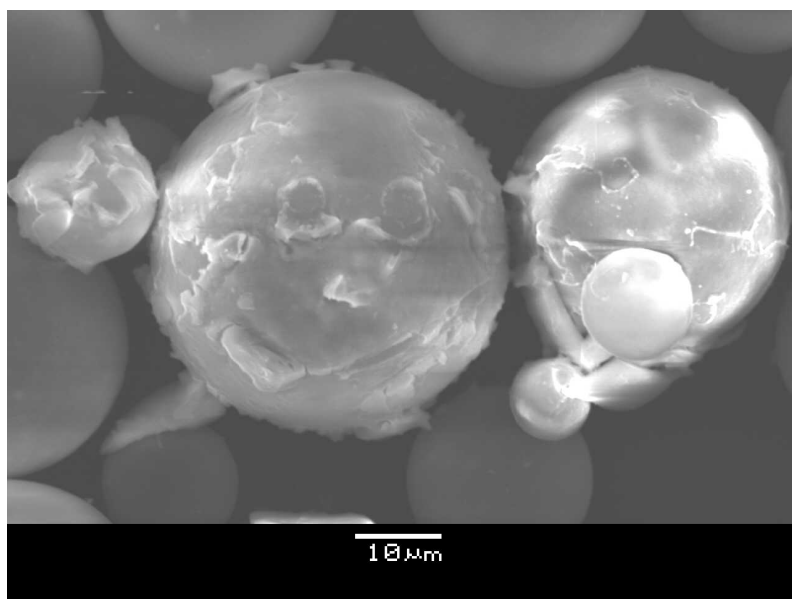


Figure 3.2 SEM image of nickel coated S60 microspheres viewed with secondary electrons at a working distance of 45mm, an accelerating voltage of 20kV, a spot size of 48, and 1400x magnification.

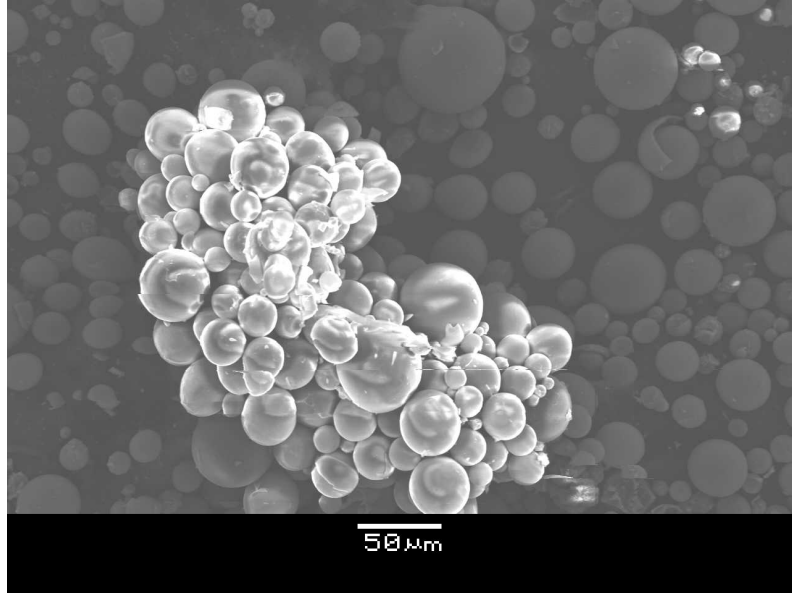


Figure 3.3 SEM image of nickel coated S60 microspheres viewed with secondary electrons at a working distance of 45mm, an accelerating voltage of 20kV, a spot size of 48, and 270x magnification.

Pycnometry measurements were taken to determine the density of the powder, which was found to be 0.664 g/cm^3 . Using this value, the measured density of the S60 microspheres, 0.584 g/cm^3 , and Equation (2.17), the approximate thickness of the nickel layer was determined to be 97nm.

3.1.1.2 Results

The particles were mixed with paraffin wax, samples were created, and the composite's electromagnetic properties were measured, as described in section 2.2.1.1. After measuring the S-parameters and using Equations (2.1) and (2.2) to find the permittivity and permeability, plots of the real permittivity (Figure 3.4), imaginary permittivity (Figure 3.5), real permeability (Figure 3.6), and imaginary permeability (Figure 3.7) as a function of frequency and volume fraction were created.

The plot of the real permittivity, Figure 3.4, shows that there is no dielectric relaxation in this frequency range and that the value of the permittivity decreases with increasing volume fraction of nickel-coated microsphere. This means that the thin nickel layer was not in the

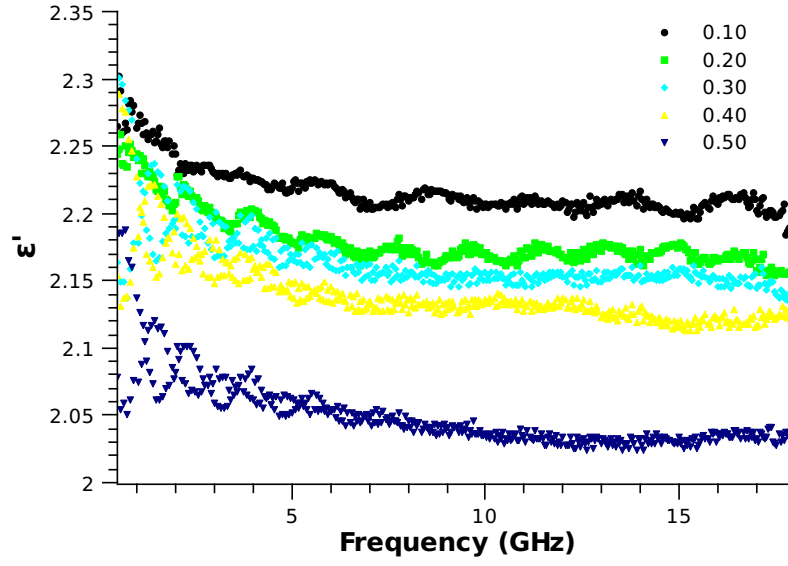


Figure 3.4 Real permittivity for nickel coated S60 microspheres as a function of frequency and volume fraction

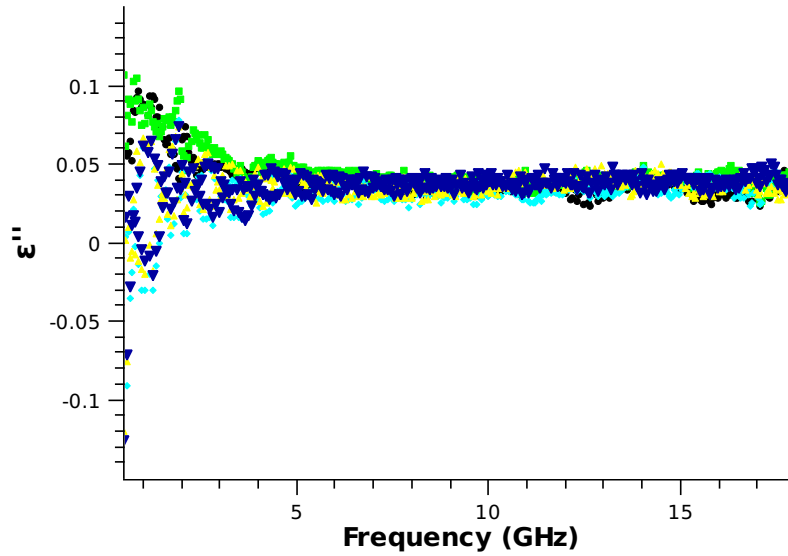


Figure 3.5 Imaginary permittivity for nickel coated S60 microspheres as a function of frequency and volume fraction

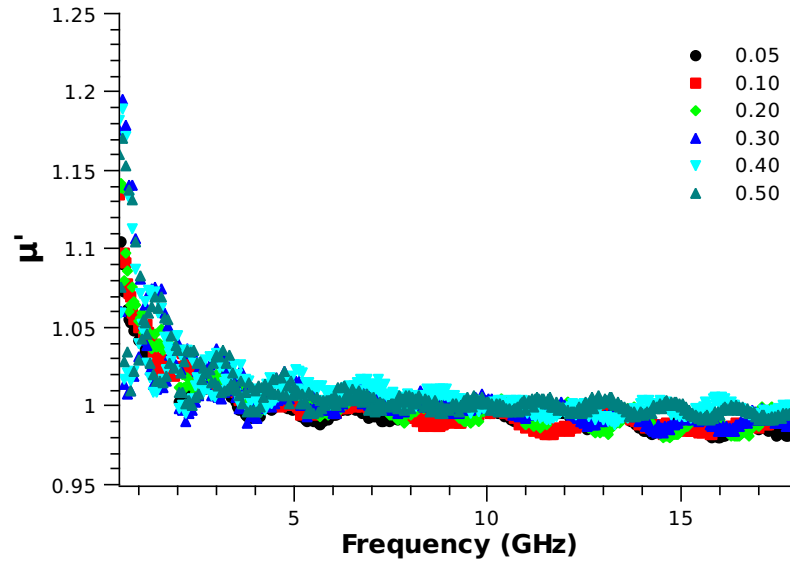


Figure 3.6 Real permeability for nickel coated S60 microspheres as a function of frequency and volume fraction

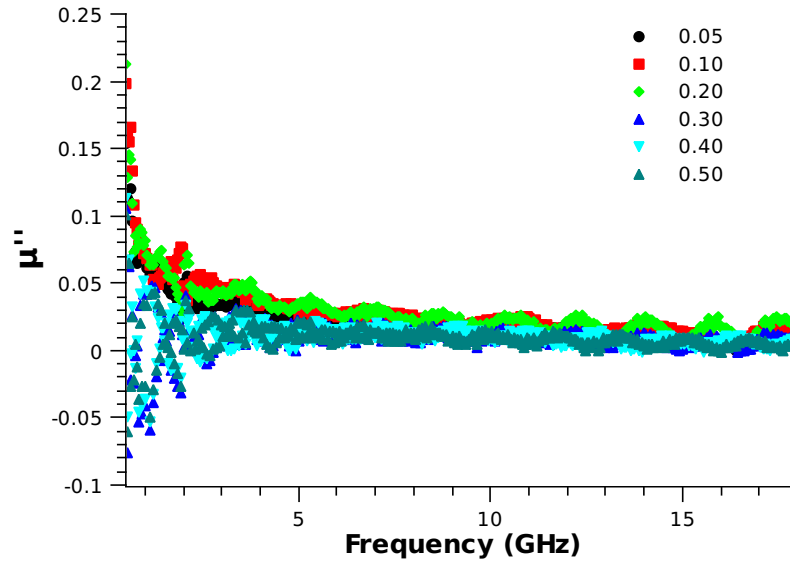


Figure 3.7 Imaginary permeability for nickel coated S60 microspheres as a function of frequency and volume fraction

correct range for dielectric relaxation. As the volume fraction of microspheres increases, so does the amount of air in the composite. As air has a permittivity of approximately one, its increase results in a decrease in the effective permittivity of the composite. The imaginary permittivity, Figure (3.5), shows that the absorption is low in this frequency range and for all volume fractions. The real and imaginary permeability (Figures 3.6 and 3.7) show that the composite is not appreciably ferromagnetic. For all measurements, uncertainties are higher at the lower end of the frequency range, as shown in [1]. These increased uncertainties result in scattering of the measurements in this region.

3.1.2 Sputtered Nickel-Coated Glass Microbubble

3.1.2.1 Overview

Another group of nickel coated microspheres, supplied by 3MTM, was also investigated, but the properties of these particles were noticeably different than those described earlier. These particles were polydisperse 3MTM C15/250 glass microspheres, sputter coated with nickel. Figure 3.8 shows the volume percent passing for seven diameters, which was made by Craig Chamberlain at 3M using a Microtrac particle size analyzer. Using this data, the cumulative size distribution was fit to a fourth order polynomial. The derivative of this function was then taken and plotted as $q_N(x)$. Using Equations (2.23) and (2.24) and taking numerical integrations using the trapezoid rule, the average diameter was determined to be $64.8\mu\text{m}$ with a standard deviation of $21.3\mu\text{m}$. This value is in very close agreement with 3M's stated average diameter of $66\mu\text{m}$.

The density of the powder was found to be 0.315 g/cm^3 , according to the method described in section 2.2.2. Using Equation (2.17), the thickness of the nickel layer was determined to be 210nm.

X-ray diffraction was used to determine more information about the coating of the particles. For these measurements a Scintag XGEN-400 diffractometer was used with a step size of 0.03° , range of $20\text{--}80^\circ$, and a speed of 1.3° per minute. The raw data of the diffraction is given as Figure 3.9.

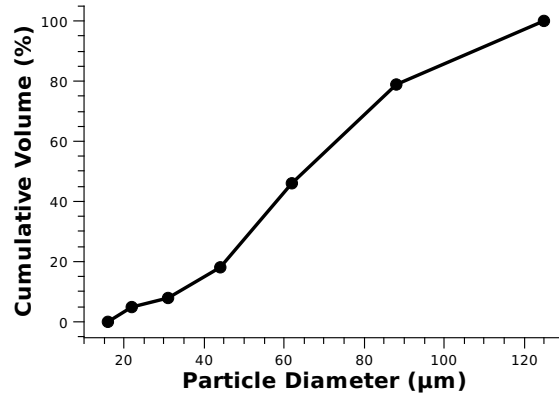


Figure 3.8 Cumulative size distribution of the nickel coated C15/250 microspheres

Using the computer program fityk, the background was removed and the peaks were fit to Pseudo-Voigt functions, resulting in the information given in Table 3.1. The shape parameter is the fraction of the peak that is described by a Lorentzian function. The analyzed data along with the fitted peaks is given as Figure 3.10. Using Equations (2.18) and (2.19) the peaks of the diffraction pattern were indexed and the lattice parameter was calculated to be 3.547\AA , which is in good agreement with the published value of 3.520\AA [43].

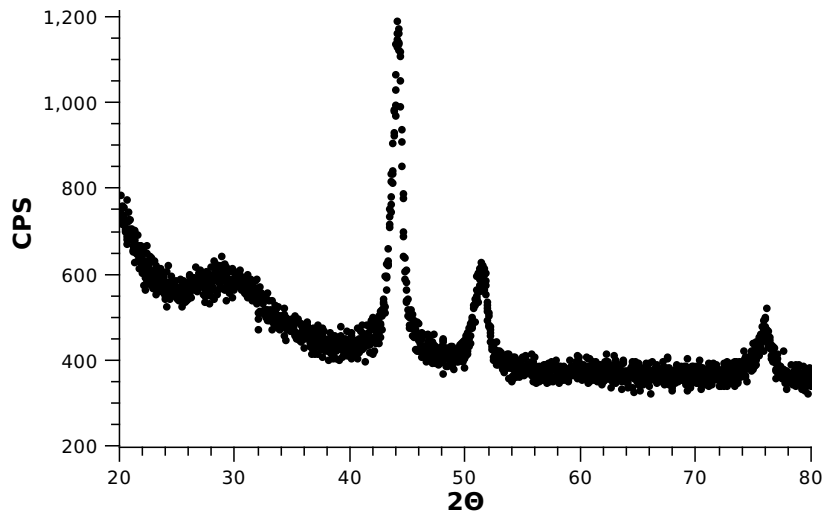


Figure 3.9 XRD pattern of Ni-C15/250 particles

Looking at the resulting data, it can be seen that the sputter coating of the nickel resulted

Table 3.1 Parameters obtained by fitting Pseudo-Voigt function to XRD data of Ni-C15/250 microspheres

Peak	hkl	Center	Height	Area	FWHW	Int. Width	Shape
1	111	44.10°	698.98	906.13	0.99	1.30	0.47
2	200	51.38°	213.86	331.61	1.34	1.55	0.18
3	220	75.96°	105.95	217.79	1.44	2.06	0.72

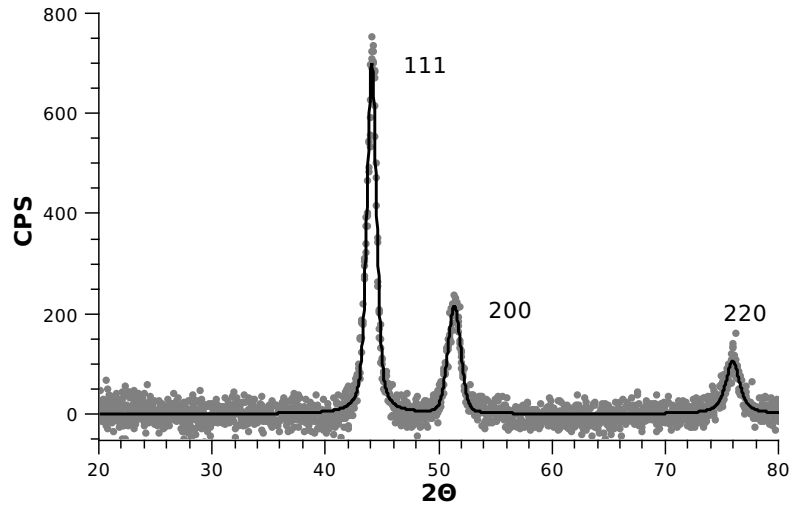


Figure 3.10 XRD pattern of Ni-C15/250 particles with background removed and fit using the Pseudo-Voigt function.

in a structure with enough crystallinity to allow Bragg diffraction. There is also evidence of an amorphous phase, shown by the first “hump” in the raw data. Whether this is due to the glass microspheres alone or if there is an amorphous component to the nickel phase is unknown since uncoated C15/250 microspheres were not available.

3.1.2.2 Results

Sample fabrication and electromagnetic measurements were completed by T.C. Maloney, which are briefly summarized here. The main emphasis is on the data analysis performed as part of this work.

The microwave electromagnetic properties of these particles were analyzed by mixing them with paraffin wax in volume fractions from 12% to 46% and taking measurements using a vector network analyzer, in the same manner as described in section 2.2.1. Figure 3.11 shows the measured real permittivity for all volume fractions as a function of frequency. The corresponding imaginary permittivity is found in Figure 3.12 increasing as a function of volume fraction, unlike the particles studied in the previous section. The real and imaginary permeabilities are given as Figures 3.13 and 3.14, respectively. As can be clearly seen in these images, there is a distinct spike in the measured real and imaginary permittivity at the higher volume fractions. These features are not due to the material properties of the composite, but due to the appearance of higher modes in the coaxial line, as discussed in section 2.2.1.4.

3.2 Monodisperse Particles

3.2.1 Electroless Nickel-Coated Glass Microsphere

3.2.1.1 Overview

The next particles studied were glass microspheres coated through electroless deposition of nickel. The particles were purchased from Mo-Sci Coporation out of Rolla, Missouri. The core particles are a soda-lime glass with 90% of the particles having a diameter between 53 and 63 μm . The particles went through a pretreatment step where they were placed in a

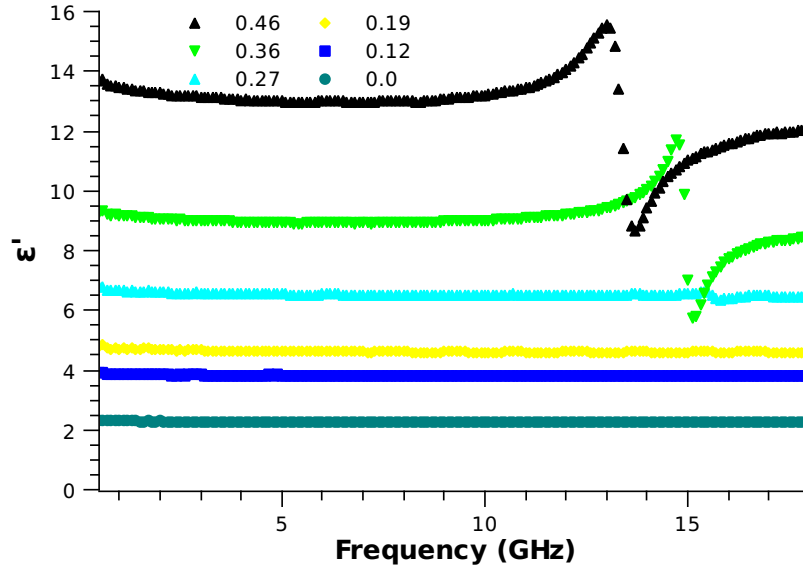


Figure 3.11 Measured ϵ' for a composite formed from nickel-coated C15/250 microspheres dispersed in paraffin wax, as a function of frequency and volume fraction

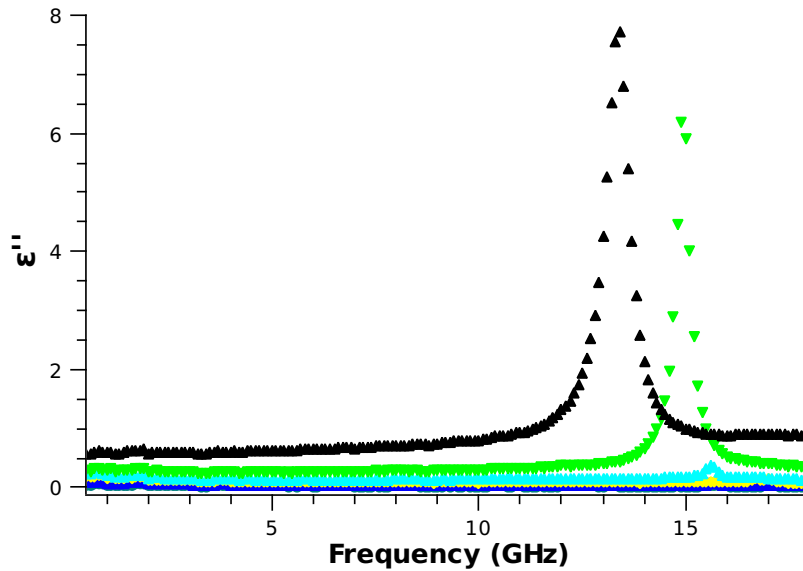


Figure 3.12 Measured ϵ'' for a composite formed from nickel-coated C15/250 microspheres dispersed in paraffin wax, as a function of frequency and volume fraction

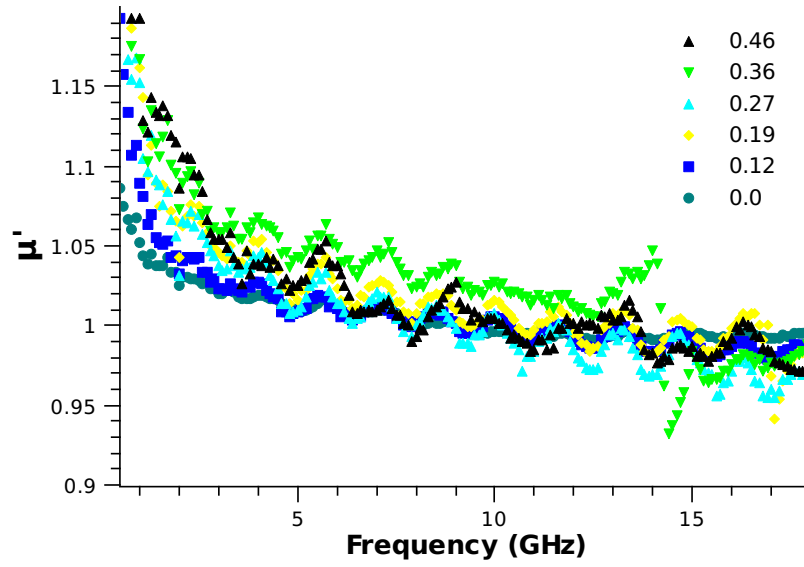


Figure 3.13 Measured μ' for a composite formed from nickel-coated C15/250 microspheres dispersed in paraffin wax, as a function of frequency and volume fraction

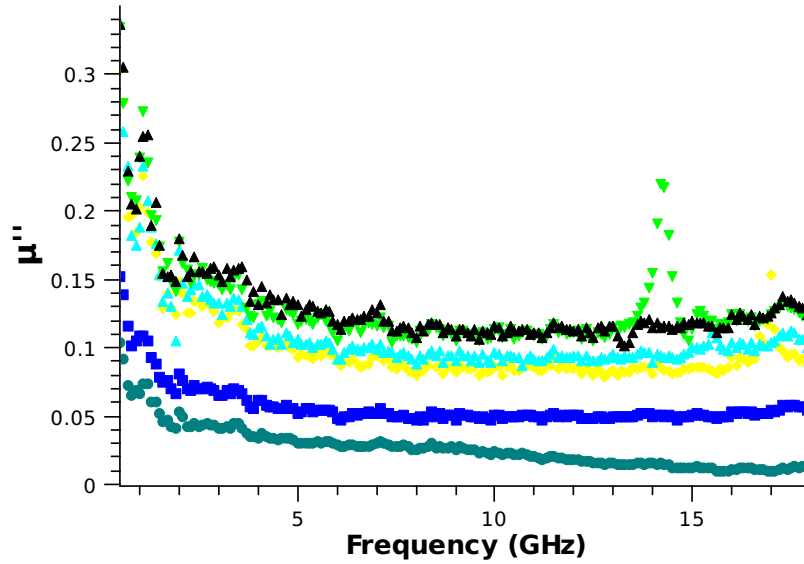


Figure 3.14 Measured μ'' for a composite formed from nickel-coated C15/250 microspheres dispersed in paraffin wax, as a function of frequency and volume fraction

solution of tin(II) chloride and hydrochloric acid, rinsed, and then placed in a solution of palladium(II) chloride to activate the non-conducting particles for deposition. The electroless nickel deposition was done using a phosphorous compound as a reducing agent, causing a small amount of phosphorous (2-10%) to remain in the deposited metal.

Using a pycnometer, the density of the coated particles was determined to be $2.597 \pm 0.024 \text{ g/cm}^3$. With a measured density of $2.445 \pm 0.024 \text{ g/cm}^3$ for the uncoated particles, Equation 2.17 was used to calculate a nickel layer thickness of 460nm.

X-ray diffraction was used to determine more information about the coating of the particles. For these measurements a Scintag XGEN-400 diffractometer was used with a step size of 0.03° , range of $20\text{-}80^\circ$, and a speed of 1.3° per minute. The diffractometer uses a Cu source with a wavelength of 1.54056 \AA . The raw data of the diffraction is given as Figure 3.15.

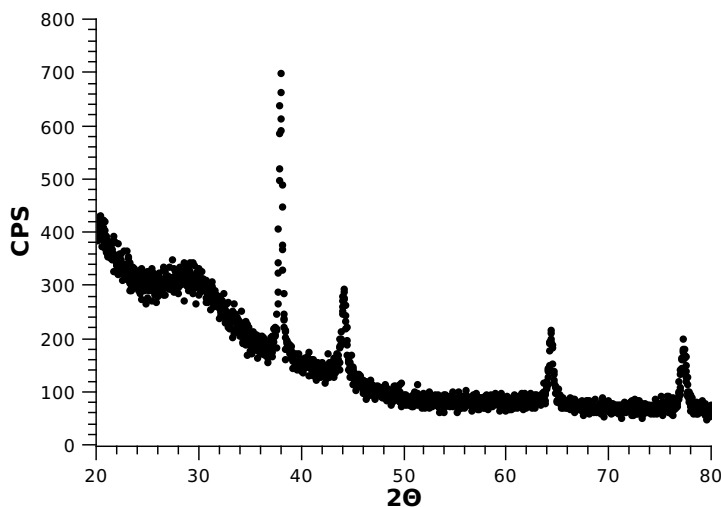


Figure 3.15 XRD pattern of nickel coated Mo-Sci particles

The background was removed and the peaks were fit to Pseudo-Voigt functions, resulting in the information given in Table 3.2. The analyzed data along with the fitted peaks is given as Figure 3.16. Due to the large number of chemical species present during the electroless reaction and the final deposited compounds being unknown, the identity of the diffraction peaks could not be defined, though the second peak appears to be that of nickel.

SEM images were taken to ensure the size distribution and to determine more information

Table 3.2 Parameters obtained by fitting Pseudo-Voigt function to XRD data of nickel coated Mo-Sci microspheres

Peak	Center	Height	Area	FWHM	Int. Width	Shape
1	38.00°	522.49	248.12	0.33	0.47	0.73
2	44.18°	160.26	123.53	0.51	0.77	0.86
3	64.37°	131.13	91.41	0.45	0.70	0.97
4	77.33°	115.80	91.14	0.61	0.79	0.44

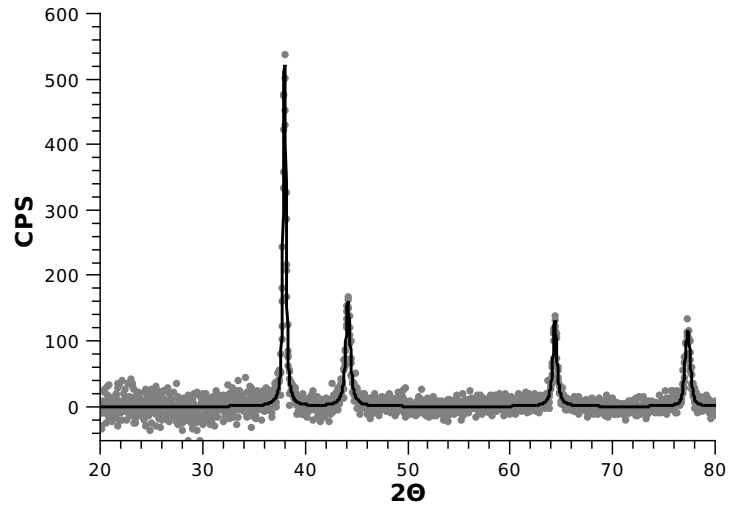


Figure 3.16 XRD pattern of nickel coated Mo-Sci particles with background removed and fit using a Pseudo-Voigt function.

about the surface of the coated particles. Figure 3.17 shows that the particles are within a tight size range, confirming the particle description given by Mo-Sci. The nickel coating appears to be continuous and mostly even, as can be seen in Figure 3.18. More detail can be seen in Figure 3.19, which shows that the surface includes a large number of irregularities and “bumps”.

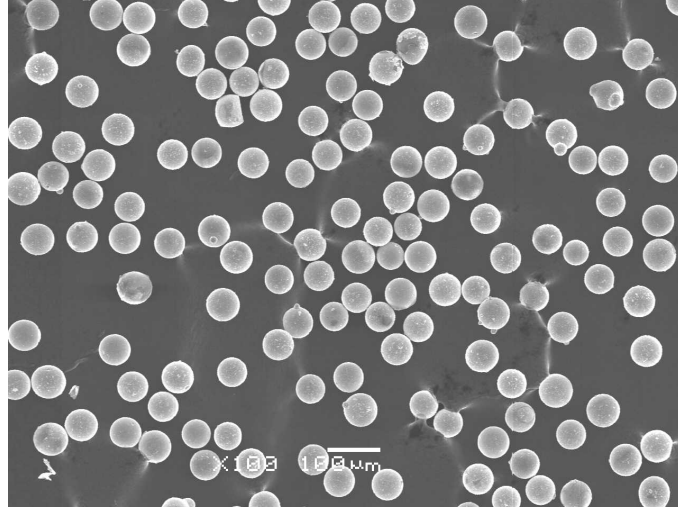


Figure 3.17 SEM image of nickel coated Mo-Sci microspheres viewed with secondary electrons at a working distance of 48mm, an accelerating voltage of 15kV, a spot size of 49, and 100x magnification.

3.2.1.2 Results

The electromagnetic properties of these particles were analyzed by mixing them with paraffin wax in volume fractions from 10-60% and taking measurements using a vector network analyzer. The measured values for the real and imaginary permittivity are given as Figures 3.20 and 3.21, while the real imaginary permeability are given as Figures 3.22 and 3.23. These values were plotted using the 10-40% volume fraction only, because the 50% and 60% measurements were highly inconsistent and the S-parameter algorithm, Equations (2.1) and (2.2), were not able to find solutions for some of the samples. As can be seen by the real and imaginary permittivity, these particles do not exhibit dielectric relaxation. This is due to the thickness of the nickel coating, which is predicted theoretically to be 10-50nm in order for dielectric relaxation to occur in the observed frequency range, instead of the measured 460nm. The real

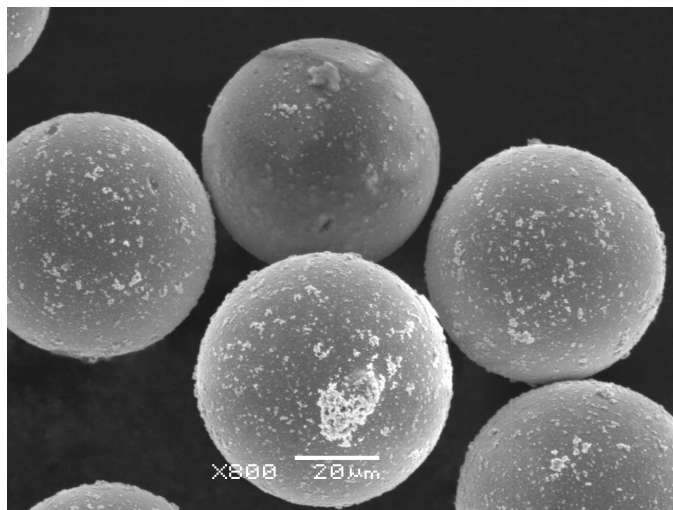


Figure 3.18 SEM image of nickel coated Mo-Sci microspheres viewed with secondary electrons at a working distance of 48mm, an accelerating voltage of 15kV, a spot size of 49, and 800x magnification.

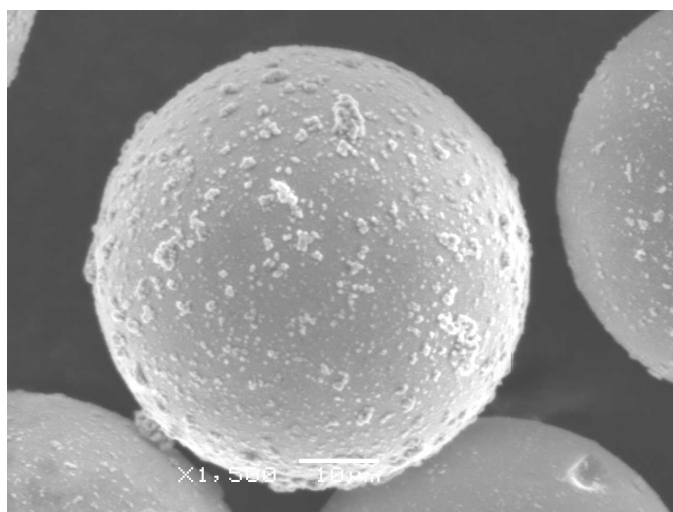


Figure 3.19 SEM image of nickel coated Mo-Sci microspheres viewed with secondary electrons at a working distance of 48mm, an accelerating voltage of 15kV, a spot size of 49, and 1500x magnification.

permeability exhibits a decrease in magnitude with volume fraction, which would suggest that the nickel is exhibiting ferromagnetic resonance. Even though the intended dielectric relaxation is not present, the appearance of ferromagnetic resonance will enhance this material's microwave absorbing capabilities.

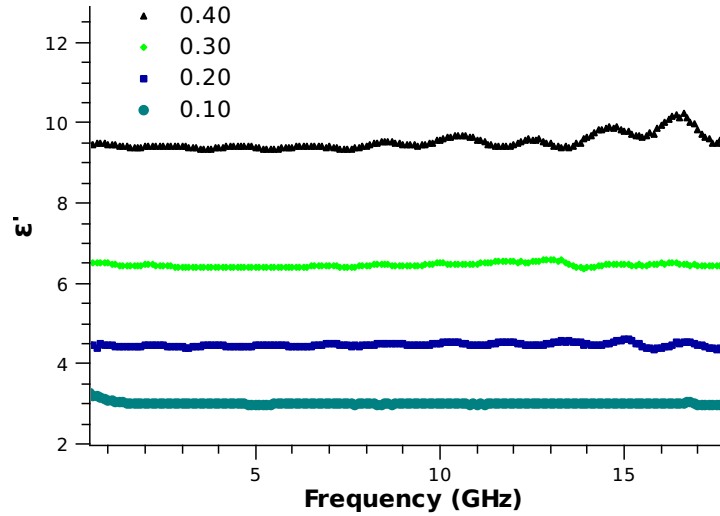


Figure 3.20 Measured ϵ' for a composite formed from nickel coated Mo-Sci microspheres dispersed in paraffin wax, as a function of frequency and volume fraction

3.3 Effective Medium Theory Comparison

3.3.1 Electroless Nickel-Coated Polydisperse Particles

The first group of particles investigated in this matter were those created by electrolessly depositing nickel onto the S60 microspheres. The measured real permittivity as a function of volume fraction was compared against the theoretical permittivity calculated using the models of Sihvola-Lindell, Harfield, and Hanai-Bruggeman, which are reviewed in sections 1.5.2 and 1.5.4. It was found that the only way for the effective medium theories to have a negative correlation between real permittivity and volume fraction was to ignore the nickel layer. The values used for the calculation are given as Table 3.3 and the result is given as Figures 3.24 and 3.25. The given error bars are one standard deviation from the average of measurements taken on three different samples of the same volume fraction. All three models found the same result

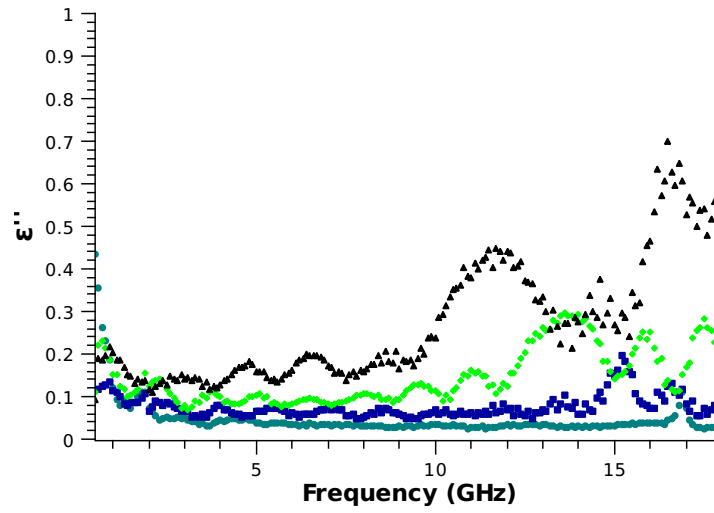


Figure 3.21 Measured ϵ'' for a composite formed from nickel coated Mo-Sci microspheres dispersed in paraffin wax, as a function of frequency and volume fraction

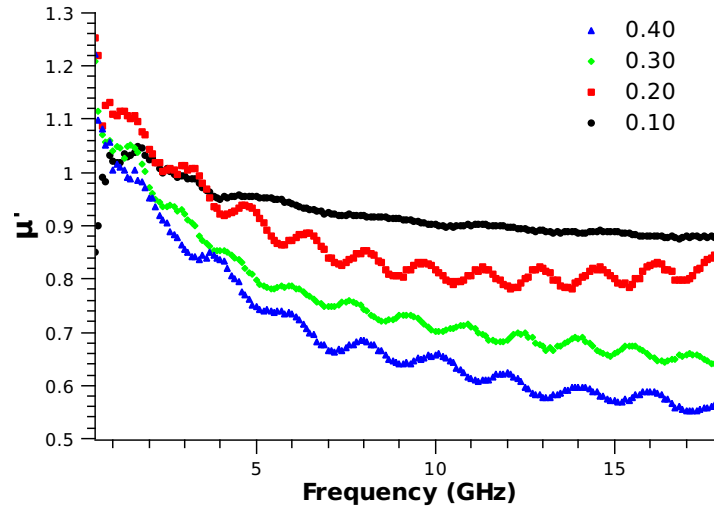


Figure 3.22 Measured μ' for a composite formed from nickel coated Mo-Sci microspheres dispersed in paraffin wax, as a function of frequency and volume fraction

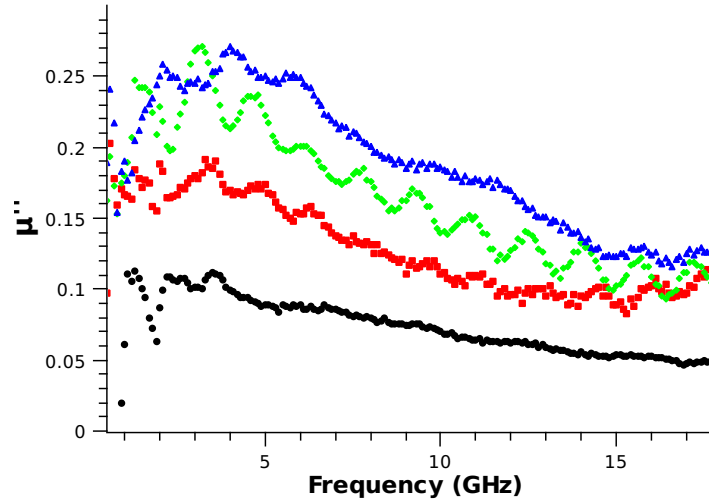


Figure 3.23 Measured μ'' for a composite formed from nickel coated Mo-Sci microspheres dispersed in paraffin wax, as a function of frequency and volume fraction

in this calculation, which were quite near the experimental values. The frequency dependence of the real permittivity was then calculated for each volume fraction and plotted along with the experimental values using the Sihvola-Lindell model, shown as Figure 3.26.

These results appear to suggest that the nickel layer has no contribution to the effective permittivity. Guided by this result, X-ray diffraction measurements were taken on these particles, which show no crystalline peaks, Figure 3.27. These measurements show that no appreciable nickel deposition took place.

3.3.2 Sputtered Nickel-Coated Polydisperse Particles

The next composite to be compared against the three effective medium theories is composed of the nickel-coated C15/250 particles from 3M. Once again, this composite was compared against the Hanai-Bruggeman, Harfield, and Sihvola-Lindell models. These three models were compared against experimental values of real permittivity at a frequency of 3GHz using the properties given in Table 3.4. The results of the calculation as a function of volume fraction of particles is given as Figures 3.28 and 3.29.

As can be seen, the Hanai-Bruggeman model describes the volume fraction dependence

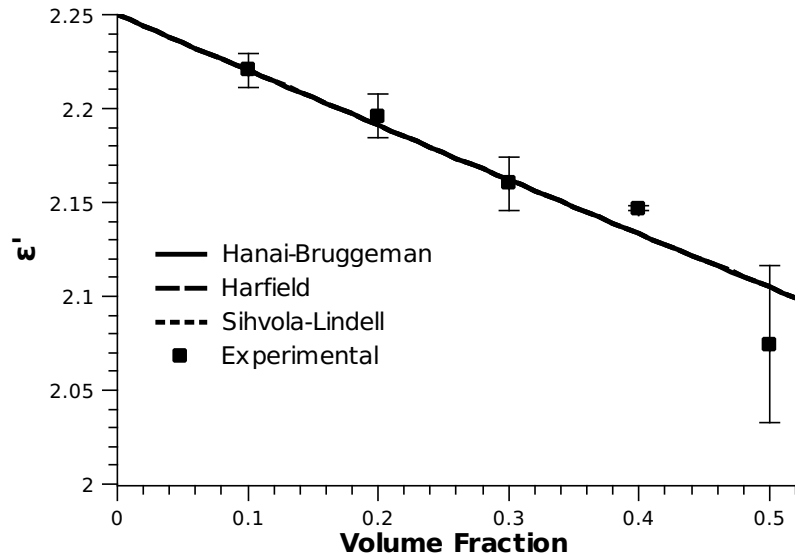


Figure 3.24 Real permittivity for nickel coated S60 microspheres as a function of volume fraction with calculated permittivity values using Hanai-Bruggeman, Harfield, and Sihvola-Lindell EMTs, assuming no coating

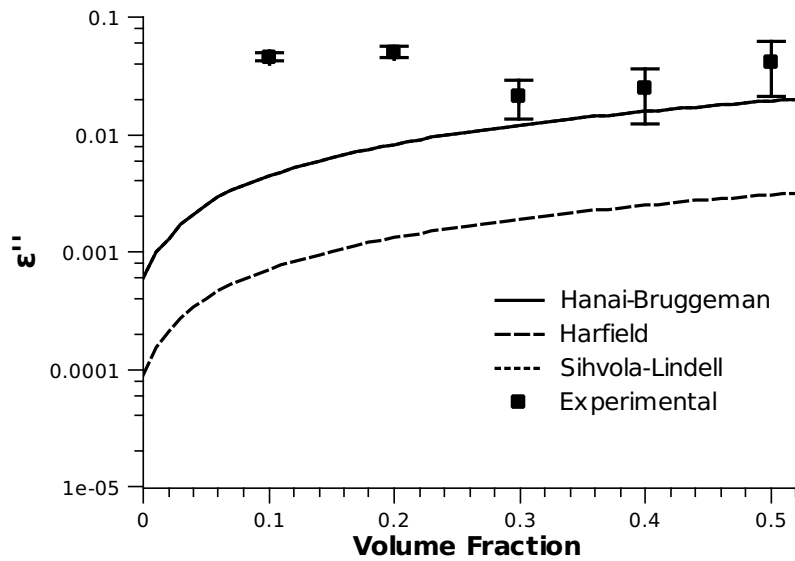


Figure 3.25 Imaginary permittivity for nickel coated S60 microspheres as a function of volume fraction with calculated permittivity values using Hanai-Bruggeman, Harfield, and Sihvola-Lindell EMTs, assuming no coating

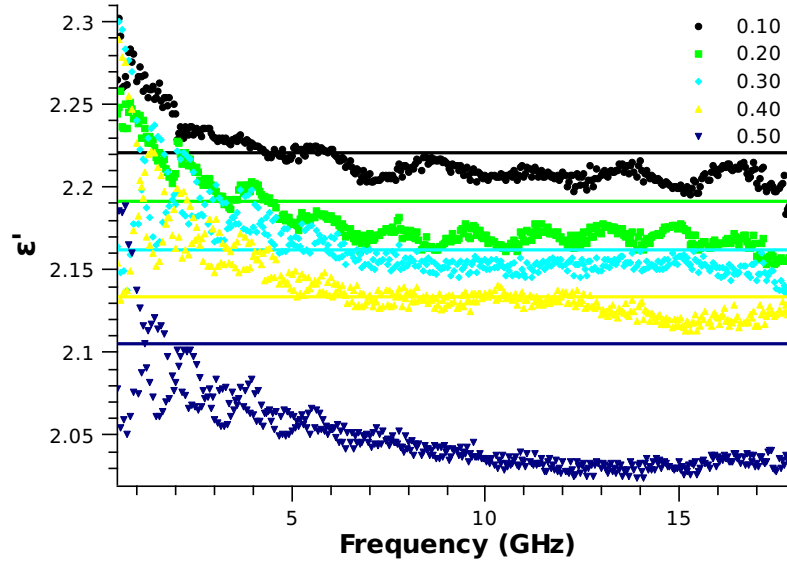


Figure 3.26 Real permittivity for nickel coated S60 microspheres as a function of frequency and volume fraction with calculated permittivity values using Equation (1.17) and Table 3.3

Table 3.3 Parameters used in Equation (1.17) to calculate real permittivity in Figure 3.26

Parameter	Value	Source
Matrix		
Material	Paraffin wax	
ϵ_m	$2.25(1-i2.5/10^4)$	[18]
Shell		
Material	Soda-lime-borosilicate glass	
a_1	$15\mu\text{m}$	[1]
ϵ_1	$6.212-i0.207$	[21]
Core		
Material	Air	
a_2	$13.7\mu\text{m}$	[1]
ϵ_2	1.00	

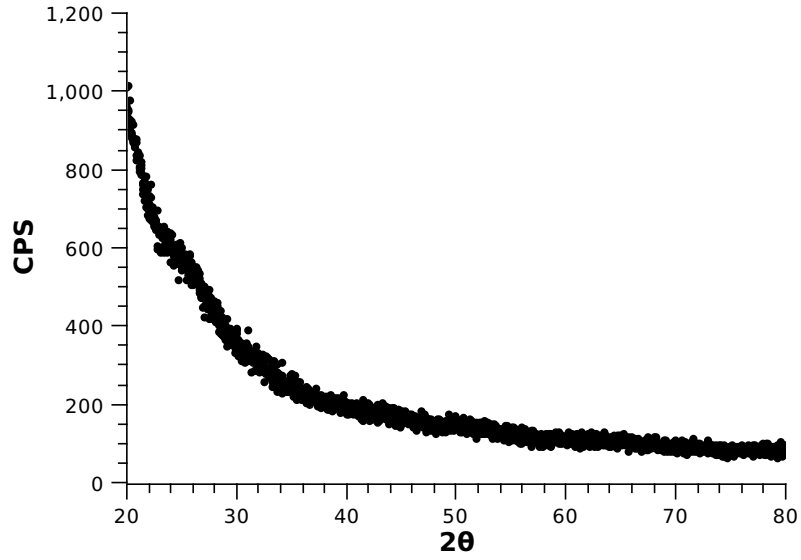


Figure 3.27 XRD pattern of electroless nickel-coated polydisperse particles

Table 3.4 Parameters used to calculate permittivity in Figures 3.28 and 3.30

Parameter	Value	Source
Matrix		
Material	Paraffin wax	
Permittivity	$2.25(1-i2.5/10^4)$	[18]
Outer shell		
Material	Nickel	
Radius	$33.21\mu\text{m}$	
Bulk conductivity	14.43 MS/m	[44]
Inner shell		
Material	Soda-lime-borosilicate glass	
Radius	$33\mu\text{m}$	
Permittivity	$6.212-i0.207$	[21]
Core		
Material	Air	
Radius	$32.2\mu\text{m}$	
Permittivity	1.00	

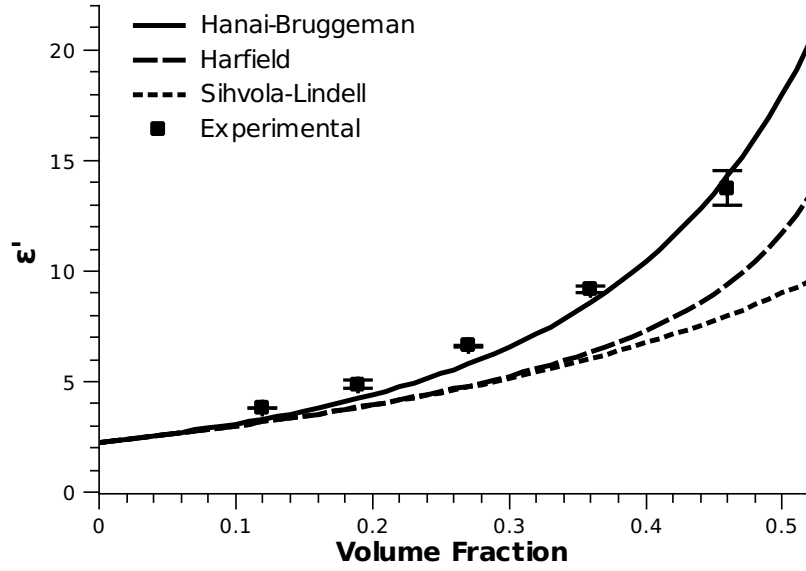


Figure 3.28 Experimental data taken at 3GHz on Ni-C15/250 microspheres in paraffin wax, compared with real permittivity calculated using the models of Sihvola-Lindell, Harfield, and Hanai-Bruggeman

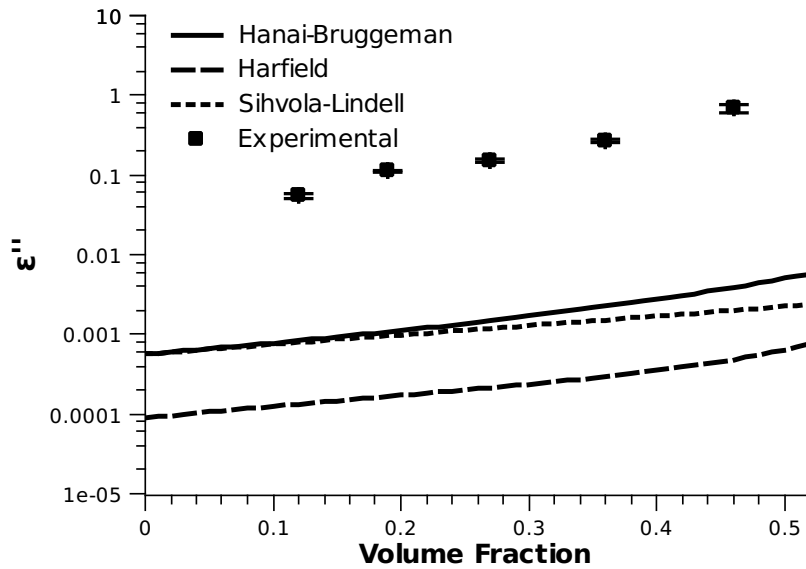


Figure 3.29 Experimental data taken at 3GHz on Ni-C15/250 microspheres in paraffin wax, compared with imaginary permittivity calculated using the models of Sihvola-Lindell, Harfield, and Hanai-Bruggeman

of the permittivity better than either the Sihvola-Lindell or Harfield model. This is most likely due to the large size distribution of the particles, which is accounted for in the Hanai-Bruggeman model. The frequency dependence of the real permittivity was then calculated for each volume fraction using the Hanai-Bruggeman model and plotted along with the experimental permittivity, shown as Figure 3.30.

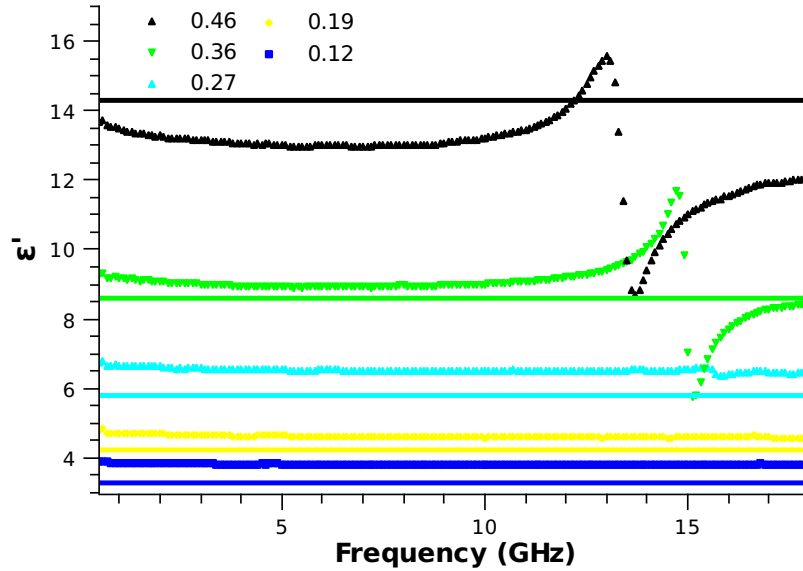


Figure 3.30 Experimental real permittivity of Ni-C15/250 microspheres along with permittivity calculated using Equation (1.28) and parameters in Table 3.4

3.3.3 Electroless Nickel-Coated Monodisperse Particles

The final composite analyzed were the nickel-coated microspheres from Mo-Sci, Inc. The parameters used for this calculation are given at Table 3.5. The theoretical permittivity was calculated using these parameters and compared against the measured permittivity values as a function of volume fraction at a frequency of 3GHz. The result of this comparison is found as Figures 3.31 and 3.32. As can be seen, the Hanai-Bruggeman model describes the real permittivity of this system as a function of volume fraction quite well. This is a surprising outcome because the Hanai-Bruggeman model inherently assumes a large size distribution of spheres in the composite. While this is appropriate for the particles studied in the previous

Table 3.5 Parameters used to calculate permittivity in Figures 3.31 and 3.33

Parameter	Value	Source
Matrix		
Material	Paraffin wax	
Permittivity	$2.25(1-i2.5/10^4)$	[18]
Shell		
Material	Nickel	
Radius	$29.46\mu\text{m}$	
Bulk conductivity	14.43 MS/m	[44]
Core		
Material	Soda-lime glass	
Radius	$29\mu\text{m}$	
Permittivity	$6.212-i0.207$	[21]

section, the Mo-Sci particles have a very narrow size distribution. The frequency dependence of the real permittivity was then calculated for each volume fraction using the Hanai-Bruggeman model and plotted along with the experimental permittivity, shown as Figure 3.33. For the lower volume fractions, it is difficult to discern the difference between the calculated values and experimental because they are very near each other.

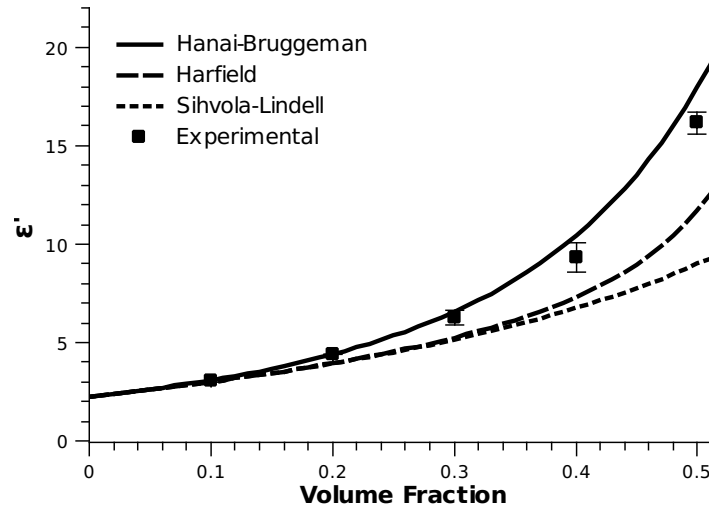


Figure 3.31 Experimental data taken at 3GHz on nickel coated Mo-Sci microspheres in paraffin wax, compared with real permittivity calculated using the model of Sihvola-Lindell, Harfield, and Hanai-Bruggeman

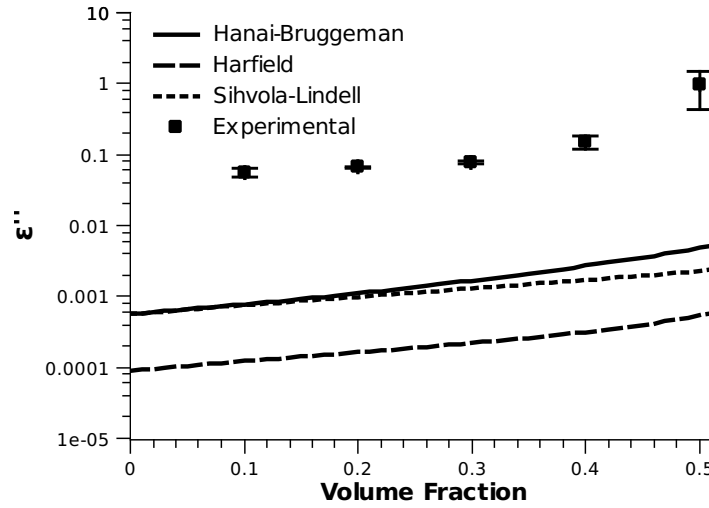


Figure 3.32 Experimental data taken at 3GHz on nickel coated Mo-Sci microspheres in paraffin wax, compared with imaginary permittivity calculated using the model of Sihvola-Lindell, Harfield, and Hanai-Bruggeman

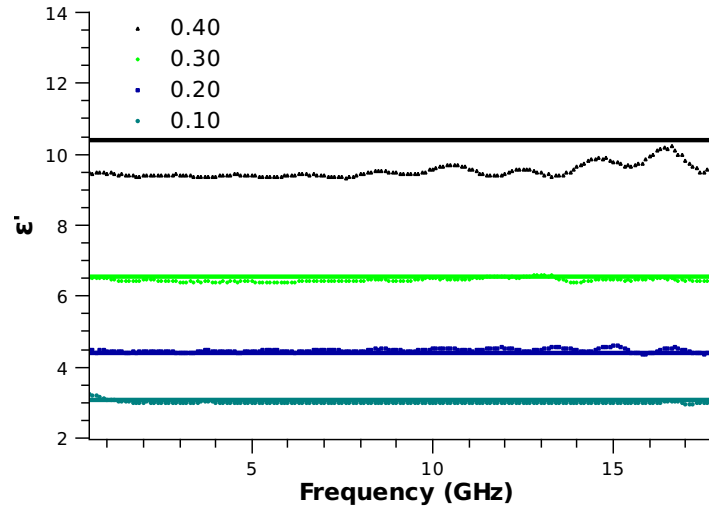


Figure 3.33 Experimental real permittivity of nickel coated Mo-Si microspheres along with permittivity calculated using Equation (1.28) and parameters in Table 3.5

CHAPTER 4. Reflection Loss Comparison

4.1 Overview

In order to compare a composite material's ability to absorb microwaves, reflection loss calculations are used, as described in section 1.3.2. In this chapter, the microwave absorbing ability of the sputtered nickel-coated particles and the electrolessly deposited nickel-coated particles will be compared against a modeled composite material and a composite material known to exhibit dielectric relaxation.

4.2 Modeled Composite

In order to establish an ideal against which the composite materials in this investigation can be compared, a reflection loss analysis was done on the calculated permittivity from section 1.5.2, Figures 1.10 and 1.11. These calculations used the Sihvola-Lindell model to calculate the effective relative permittivity where $\epsilon_m = 2.25(1 - i2.5/10^4)$, $\epsilon_1 = 1 - i\frac{\sigma}{\omega\epsilon_0}$, $\sigma = 10^4$ S/m, $\epsilon_2 = 6.212 - i0.207$, $a_1 = 30.015\mu\text{m}$, and $a_2 = 30\mu\text{m}$. This composite exhibits dielectric relaxation in the 0.5-18GHz frequency range. Using Equation (1.1), the reflection loss as a function of thickness and frequency was calculated for volume fractions between 0.10 and 0.50. The reflection loss contour for the 0.50 volume fraction is given as Figure 4.1. With -30dB as the necessary loss for a good absorber, this model composite shows a large region of thicknesses and frequencies where adequate microwave absorption occurs. A plot of the minimum reflection loss for multiple volume fractions as a function of frequency is given as Figure 4.2. This shows that both the 0.40 and 0.50 volume fractions have reflection losses that reach a level necessary for adequate absorption.

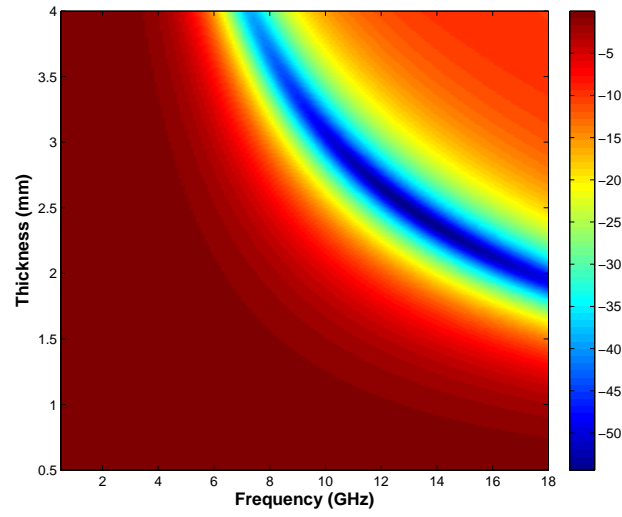


Figure 4.1 Reflection loss contour for 0.50 volume fraction on model composite calculated using the Sihvola-Lindell model where $\epsilon_m = 2.25(1 - i2.5/10^4)$, $\epsilon_1 = 1 - i\frac{\sigma}{\omega\epsilon_o}$, $\sigma = 10^4$ S/m, $\epsilon_2 = 6.212 - i0.207$, $a_1 = 30.015\mu\text{m}$, and $a_2 = 30\mu\text{m}$

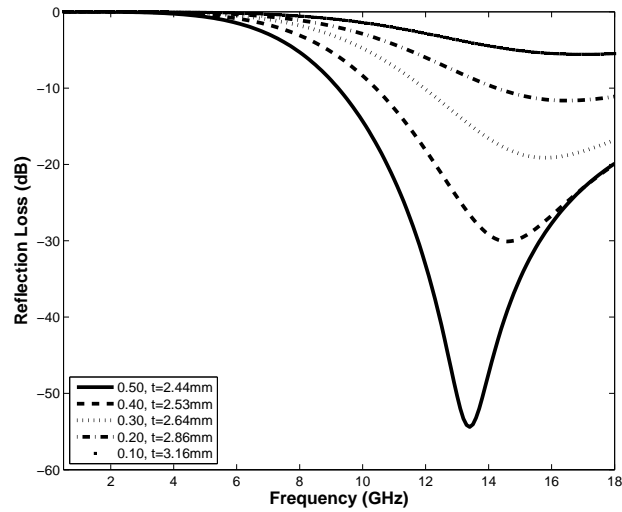


Figure 4.2 Minimum reflection loss for model composite described in section 1.5.2

4.3 Composite Exhibiting Dielectric Relaxation

Now calculations of reflection loss are given for a composite material that has been shown to exhibit dielectric relaxation in the microwave frequency range [45]. This composite was composed of a hollow glass shell with a radius of $30\mu\text{m}$ that was coated with tungsten and had an outer layer of alumina, each with a nominal thickness of 3nm. The relative real and imaginary permittivity measurements for these particles is given as Figures 4.3 and 4.4. The reflection loss contour for the 0.60 volume fraction is given as Figure 4.5. A plot of the minimum reflection loss for multiple volume fractions as a function of frequency is given as Figure 4.6. This shows that this composite has sufficient reflection loss for both the 0.50 and 0.60 volume fraction.

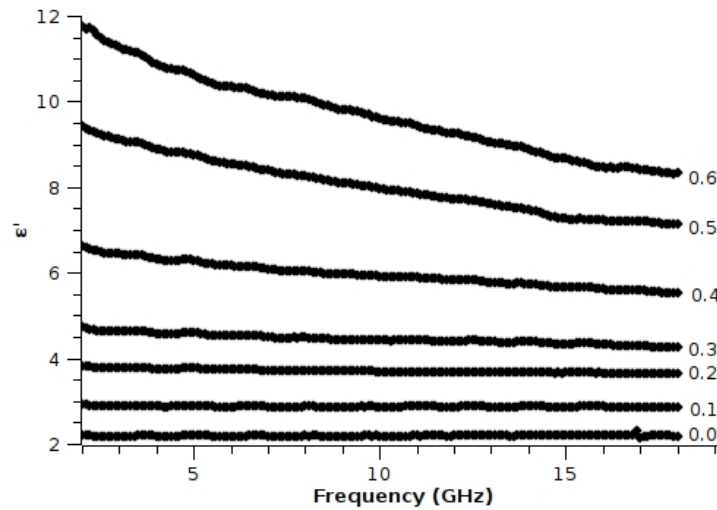


Figure 4.3 Measured ϵ' for a composite formed from a hollow glass core, coated with tungsten and an outer layer of alumina, which exhibits dielectric relaxation [45]

4.4 Sputtered Nickel-Coated Glass Microbubble

The first material from this study to be investigated are the C15/250 microspheres that have a layer of nickel sputter coated. Due to the appearance of higher modes in the transmission line during measurements, the experimental permittivity and permeability near these features

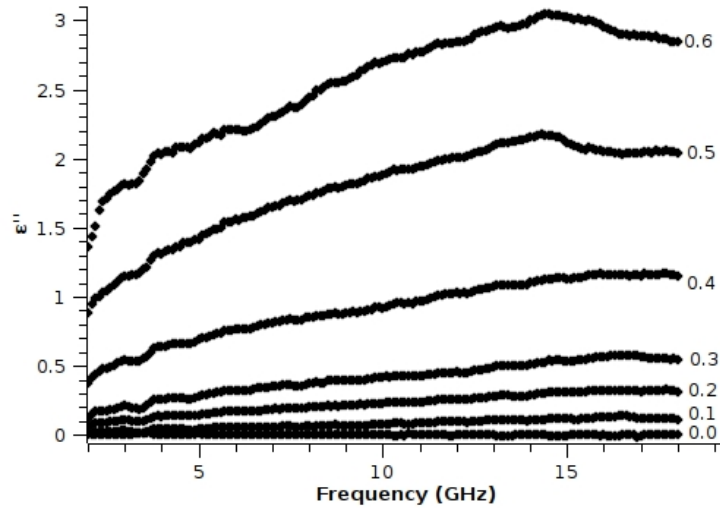


Figure 4.4 Measured ϵ'' for a composite formed from a hollow glass core, coated with tungsten and an outer layer of alumina, which exhibits dielectric relaxation [45]

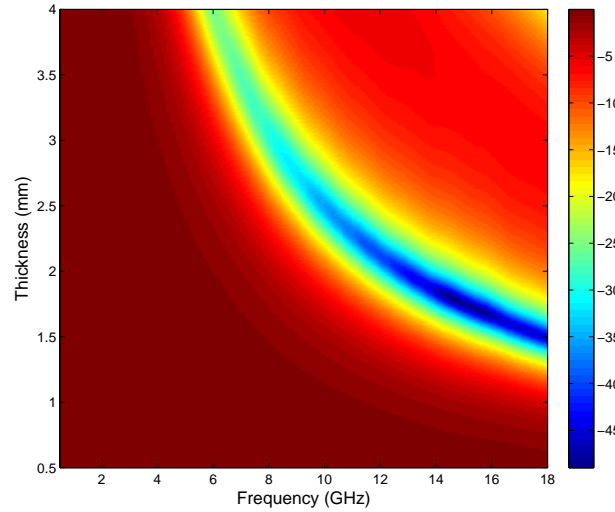


Figure 4.5 Reflection loss contour for 0.60 volume fraction of a composite with a hollow glass core, coated with tungsten and an outer layer of alumina, which exhibits dielectric relaxation

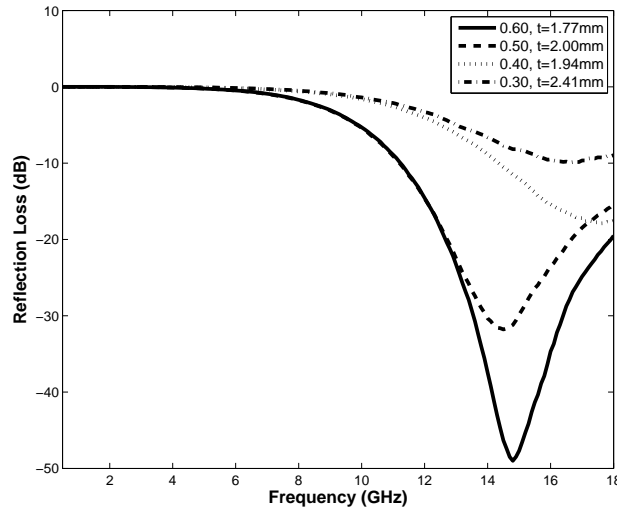


Figure 4.6 Minimum reflection loss for a composite a with hollow glass core, coated with tungsten and an outer layer of alumina, which exhibits dielectric relaxation for multiple volume fractions

could not be used for reflection loss calculations. The large features in the real and imaginary permittivity would result in a reflection loss substantially higher than the composite's actual microwave absorbing ability. Instead, the reflection loss calculation was done from 0.5 to 11GHz, ensuring that the calculation was clear of the effects of the higher modes. The resulting reflection loss contour for the 0.46 volume fraction is shown as Figure 4.7. The minimum reflection loss for multiple volume fractions as a function of frequency is given as Figure 4.8. The highest volume fraction, 0.46, reaches a reflection loss of approximately -25dB, which is short of the necessary -30dB to be considered an adequate microwave absorbing material.

4.5 Electroless Nickel-Coated Glass Microsphere

The final composite material examined are the glass microspheres that were electrolessly deposited with nickel by Mo-Sci Corporation. The calculated reflection loss contour for the 0.30 volume fraction is shown as Figure 4.9. The minimum reflection loss for multiple volume fraction as a function of frequency is given as Figure 4.10. The 0.40 volume fraction was not included in this investigation because the noise in the measurement resulted in unrealistic reflection loss values. The 0.30 volume fraction reaches a reflection loss value of -25dB near

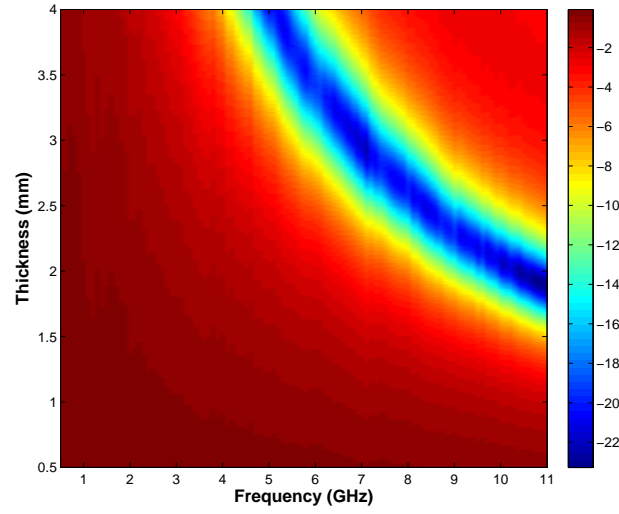


Figure 4.7 Reflection loss contour for 0.46 volume fraction of nickel-coated C15/250 particles

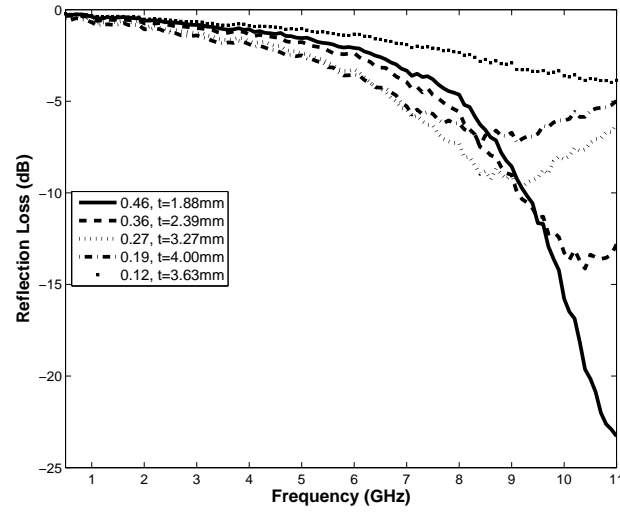


Figure 4.8 Minimum reflection loss for nickel-coated C15/250 particles for multiple volume fractions

9.5GHz, which is below the necessary value of -30dB to be considered a good absorber.

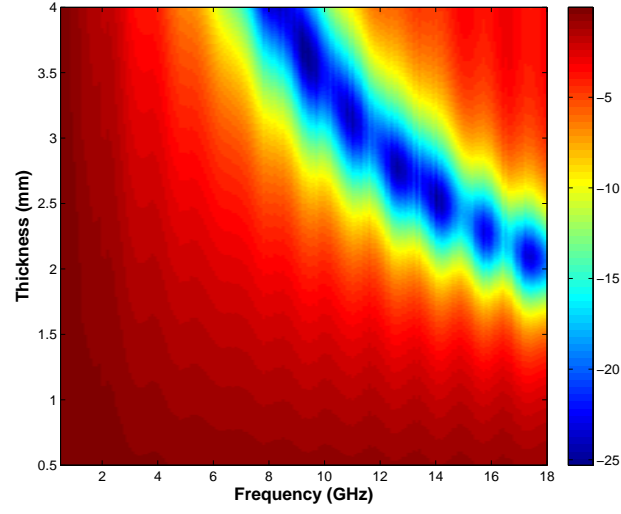


Figure 4.9 Reflection loss contour for 0.30 volume fraction of nickel-coated Mo-Sci particles

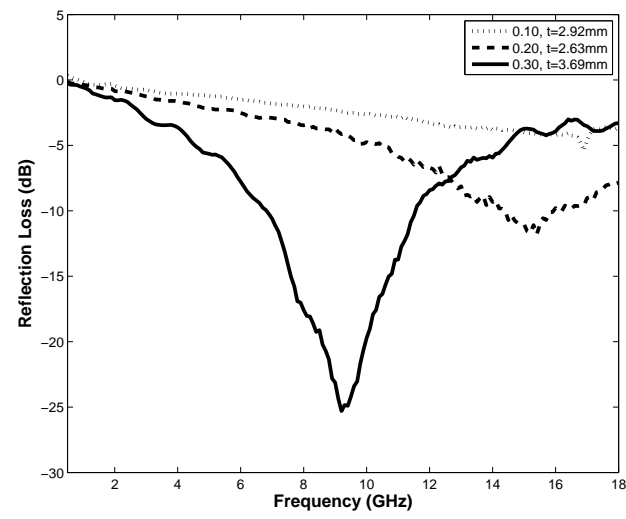


Figure 4.10 Minimum reflection loss for nickel-coated Mo-Sci particles for multiple volume fractions

CHAPTER 5. Conclusion

Comparing the calculated reflection loss for the three composite materials against the modeled reflection loss, the alumina and tungsten coated composite that exhibits dielectric relaxation has the greatest microwave absorbing ability. This should not be surprising, considering the appearance of dielectric relaxation was the intended means to bring about absorption. The electroless nickel-coated particles produce the composite with the greatest absorbing ability of the materials studied in detail in this investigation. The 0.30 volume fraction particles in this calculation were not able to reach the necessary -30dB to be considered an adequate absorber, but it can safely be assumed that the 0.40 and higher volume fraction would have the necessary loss to extend beyond this value.

It is difficult to form a complete conclusion regarding the reflection loss data from the sputtered nickel microspheres. Because of the appearance of higher order modes causing apparent resonance in the measured relative permittivity and permeability data, the measured permittivity and permeability could only be used up to 11GHz. Even with this small window available, it is shown that this composite has a lower microwave absorbing ability than a composite containing the electroless coated monodisperse particles. The 0.46 volume fraction composite can be assumed to reach a reflection loss of -25dB slightly above 11GHz, which is roughly equal to the absorption achieved with the monodisperse, electroless coated particles using a lower volume fraction. While both of these particles do absorb some of the incident electromagnetic radiation, they do not absorb to the degree possible if they showed dielectric relaxation in this frequency range.

After comparing the Sihvola-Lindell, Harfield, and Hanai-Bruggeman effective medium theories against three different composite mixtures, it was found that the Hanai-Bruggeman model

correlated to experimental values the best. While all of the models correctly predicted the real permittivity of the electroless nickel-coated polydisperse particles that were subsequently shown by XRD to have no significant component of crystalline nickel (Figure 3.24), the Hanai-Bruggeman model clearly reflected the experimental results in both the sputtered polydisperse (Figure 3.28) and electroless nickel-coated monodisperse particles (Figure 3.31) better than the other models. While this result is foreseeable with the polydisperse particles, since this model inherently assumes a wide size range of particles, it is surprising that the monodisperse particles are described equally as well. None of the models were able to effectively predict the imaginary permittivity, but this is a common problem in studies comparing effective medium theories to experimental data [46], where the theoretical values are much lower than experimental values.

The actual process of creating these composite materials requires more investigation. The electroless deposition process was found to be challenging to control when working with the thicknesses desired. This process is mainly used for depositions where coatings in the micron or greater scale are used, not in the nanometer range. Further steps should be taken to slow down the deposition process, either through lowering the temperature, adjusting the pH, or changing the chemicals used entirely. The problem of the deposited nickel flaking off should also be addressed in order to ensure a consistent coating on every particle. Slowing down the deposition should help with this problem, but a change in the deposition chemistry is more likely to be necessary.

If this method is not deemed a suitable means of deposition in the nanometer scale, other methods should be investigated. Chemical methods are the most likely way to give the spherical particles an even coating, as opposed to physical methods such as evaporation or sputtering. Physical methods require the particles to be in motion while the deposition is occurring so that all angles of the sphere are exposed to the deposition process, which cannot ensure an even and equal coating on every particle. Once greater control over the deposition process is achieved, a more in-depth study of the relationship between layer thickness and dielectric response can commence.

REFERENCES

- [1] Youngs I J, Bowler N, Lymer K P and Hussain S 2005 *J. Phys. D: Appl. Phys.* **38** 188–201
- [2] Youngs I J, Bowler N and Ugurlu O 2006 *J. Phys. D: Appl. Phys.* **39** 1312–1325
- [3] CTIAorg 13 November 2007 Wireless quick facts - mid-year figures URL http://www.ctia.org/media/industry_info/index.cfm/AID/10323
- [4] Ku H S 2006 *Progress in Electromagnetics Research, PIER* **66** 267–285
- [5] Lee W and Springer G 1984 *Journal of Composite Materials* **18** 387–409
- [6] Pae P 2004 *Los Angeles Times*
- [7] Meshram M R, Agrawal N K, Sinha B and Misra P 2004 *Journal of Magnetism and Magnetic Materials* **271** 207–214
- [8] Kim D Y, Chung Y C, Kang T W and Kim T C 1996 *IEEE Transactions on Magnetics* **32**(2) 555
- [9] Neelankanta P 1995 *IEEE Transactions on Microwave Theory and Techniques* **43**(6) 1381–1383
- [10] Lax B and Button K J 1962 *Microwave Ferrites and Ferrimagnetics* (McGraw-Hill)
- [11] Soohoo R F 1985 *Microwave Magnetics* (Harper & Row Publishers:New York)
- [12] Lagarkov A, Razanov K, Simonov N and Starostenko S 2005 *Microwave Permeability of Magnetic Films* vol IV of *Handbook of Advanced Magnetic Materials* (Springer) chap 13, pp 414–445

- [13] Fröhlich H 1949 *Theory of Dielectrics* (Clarendon Press)
- [14] Kasap S O 2005 *Principles of Electronic Materials and Devices* 3rd ed (McGraw-Hill)
- [15] Raju G G 2003 *Dielectrics in Electric Fields* (Marcel Dekker, Inc.)
- [16] Bowler N 2006 *IEEE Transactions on Dielectrics and Electrical Insulation* **13**(4) 703–711
- [17] Maxwell Garnett J 1904 *Philosophical Transactions of the Royal Society of London* **203** 385–420
- [18] von Hippel A 1954 *Dielectric Materials and Applications* (New York: Wiley)
- [19] Ramo S, Whinnery J and van Duzer T 1984 *Fields and Waves in Communication Electronics* (New York: Elsevier)
- [20] Sihvola A H and Lindell I V 1992 in A Priou, ed, *Dielectric Properties of Heterogeneous Materials* (New York: Elsevier) pp 101–51
- [21] Grignon R, Afsar M N, Wang Y and Butt S 2003 *Instrumentation and Measurement Technology Conference*
- [22] Eckertová L 1986 *Physics of Thin Films* second edition ed (Plenum Press)
- [23] Le Bas J 1969 *C. R. Acad. Sci.* **268** 262
- [24] Angadi M A and Udachan L A 1981 *Thin Solid Films* **79** 149–153
- [25] De Vries J W C 1987 *Thin Solid Films* **150** 209–215
- [26] Mayadas A F, Shatzkes M and Janak J F 1969 *Applied Physics Letters* **14**(11) 345–347
- [27] Mayadas A F and Shatzkes M 1970 *Phys. Rev. B* **1**(4) 1382–1389
- [28] Lim J W, Mimura K and Isshiki M 2003 *Applied Surface Science* **217** 95–99
- [29] Harfield N 2000 *Journal of Material Science* **35** 5809
- [30] Bowler N, Fischer N L and Maloney T C In Preparation *Applied Physics Letter*

- [31] Watanabe T 2004 *Nano-Plating: Microstructure Control Theory of Plated Film and Data Base of Plated Film Microstructures* (Boston: Elsevier)
- [32] Mallory G O 1990 in G O Mallory and J B Hajdu, eds, *Electroless Plating: Fundamentals and Applications* (Orlando, FL: American Electroplaters and Surface Finishers Society) chap 2, pp 57–99
- [33] Colaruotolo J and Tramontana D 1990 in G O Mallory and J B Hajdu, eds, *Electroless Plating: Fundamentals and Applications* (Orlando, FL: American Electroplaters and Surface Finishers Society) chap 8, pp 207–227
- [34] Baudrand D W 2002 in *ASM Handbook* (ASM International) second edition ed
- [35] Law H, Mattoe C, Thomson J J, Smith T and Zappula R 1991 *Electronics Manufacturing Technology Symposium, 1991., Eleventh IEEE/CHMT International* pp 379–382
- [36] Jaeger R C 2002 *Introduction to Microelectronic Fabrication* 2nd ed vol V of *Modular Series on Solid State Devices* (Prentice Hall)
- [37] Baker-Jarvis J 1990 Transmission/reflection and short-circuit line permittivity measurements Tech. Rep. 1341 NIST
- [38] Nicolson A and Ross G 1970 *IEEE Transactions on Instrumentation and Measurement* **19**(4) 377–382
- [39] Weir W 1974 *Proceedings of the IEEE* **62**(1) 33–36
- [40] Abram E 2007 *Electromagnetic materials characterization of ferromagnetic composites at microwave frequencies* Master’s thesis Iowa State University
- [41] Pecharsky V K and Zavalij P Y 2005 *Fundamentals of Powder Diffraction and Structural Characterization of Materials* (Springer)
- [42] Rahaman M N 2003 *Ceramic Processing and Sintering* 2nd ed (Marcel Dekker, Inc.)
- [43] Ashcroft N W and Mermin N D 1976 *Solid State Physics* (Brooks/Cole)

- [44] Weast R, ed 1977 *CRC Handbook of Chemistry and Physics* (CRC Press)
- [45] Maloney T C, Bowler N and Fischer N L *IEEE Transactions on Dielectrics and Electrical Insulation* Accepted for Publication
- [46] Merrill W M, Diaz R E, LoRe M M, Squires M C and Alexopoulos N G 1999 *IEEE Transactions on Antennas and Propagation* **47**(1) 142

ACKNOWLEDGMENTS

I would like to first thank Dr. Nicola Bowler for her guidance, patience, and encouragement during my graduate studies. Her contagious enthusiasm has always inspired me to work hard.

I would also like to thank Dr. Xiaoli Tan and Dr. Jaeyoun Kim for agreeing to be on my committee and for their advice and suggestions along the way. Also, thank you to Dr. Steve Martin and Dr. Xiaoli Tan for allowing me to use their lab space for my research.

A special thank you goes to all my friends and colleagues for their friendship, engaging conversation, and humor. They have changed my college experience for the better every step of the way.

I would especially like to thank my parents, Greg and Kathy, my brothers, grandparents, and the rest of my family for their unconditional support during my time at college. Even though you may not understand my words, know my intention: it was always just to make you proud.

Finally, I thank God for giving me the ability to discover and appreciate the beauty of His creation. In te, Domine, speravi: non confundar in aeternum.